Stem Cell Reports
Article

ISSCR

OPEN ACCESS

Human Pluripotent Stem Cell-Derived Cardiac Tissue-like Constructs for Repairing the Infarcted Myocardium

Junjun Li,[1,2,6] Itsunari Minami,[1,3,6] Motoko Shiozaki,[3] Leqian Yu,[1,2] Shin Yajima,[3] Shigeru Miyagawa,[3] Yuji Shiba,[4] Nobuhiro Morone,[1,7] Satsuki Fukushima,[3] Momoko Yoshioka,[1] Sisi Li,[1,5] Jing Qiao,[1,2] Xin Li,[1] Lin Wang,[1] Hidetoshi Kotera,[2] Norio Nakatsuji,[1] Yoshiki Sawa,[3,*] Yong Chen,[1,5,*] and Li Liu[1,2,*]

[1]Institute for Integrated Cell-Material Sciences (WPI-iCeMS), Kyoto University, Yoshida-Ushinomiya-cho, Sakyo-ku, Kyoto 606-8501, Japan
[2]Nanometorics Laboratory, Department of Micro Engineering, Kyoto University, Katsura, Nishi-ku, Kyoto 615-8540, Japan
[3]Department of Cardiovascular Surgery, Osaka University Graduate School of Medicine, 2-2 Yamadaoka, Suita, Osaka 565-0871, Japan
[4]Institute for Biomedical Sciences, Department of Cardiovascular Medicine, Shinshu University, 3-1-1 Asahi, Matsumoto, Nagano 390-8621, Japan
[5]PASTEUR, Département de chimie, école normale supérieure, PSL Research University, Sorbonne Universités, UPMC Université Paris 06, CNRS, 75005 Paris, France
[6]Co-first author
[7]Present address: MRC Toxicology Unit, Hodgkin Building, University of Leicester, PO Box 138, Lancaster Road, Leicester LE1 9HN, UK
*Correspondence: sawa@surg1.med.osaka-u.ac (Y.S.), yong.chen@ens.fr (Y.C.), liu@me.kyoto-u.ac.jp (L.L.)
https://doi.org/10.1016/j.stemcr.2017.09.007

SUMMARY

High-purity cardiomyocytes (CMs) derived from human induced pluripotent stem cells (hiPSCs) are promising for drug development and myocardial regeneration. However, most hiPSC-derived CMs morphologically and functionally resemble immature rather than adult CMs, which could hamper their application. Here, we obtained high-quality cardiac tissue-like constructs (CTLCs) by cultivating hiPSC-CMs on low-thickness aligned nanofibers made of biodegradable poly(D,L-lactic-co-glycolic acid) polymer. We show that multi-layered and elongated CMs could be organized at high density along aligned nanofibers in a simple one-step seeding process, resulting in upregulated cardiac biomarkers and enhanced cardiac functions. When used for drug assessment, CTLCs were much more robust than the 2D conventional control. We also demonstrated the potential of CTLCs for modeling engraftments *in vitro* and treating myocardial infarction *in vivo*. Thus, we established a handy framework for cardiac tissue engineering, which holds high potential for pharmaceutical and clinical applications.

INTRODUCTION

Human pluripotent stem cells (hPSCs), including human embryonic stem cells (hESCs) and human induced pluripotent stem cells (hiPSCs), can be differentiated into cardiomyocytes (hPSC-CMs), which offer a number of advantages for drug development as well as for myocardial regeneration (Matsa and Denning, 2012; Liang et al., 2013; Chong et al., 2014; Kimbrel and Lanza, 2015; Feric and Radisic, 2016; Shinozawa et al., 2017). However, although high-purity CM differentiation can be achieved (Minami et al., 2012; Lian et al., 2013; Burridge et al., 2014), the hPSC-CMs derived under normal conditions are randomly distributed and resemble immature rather than adult CMs, as demonstrated by their morphological and functional characteristics (Snir et al., 2003; Robertson et al., 2013; Matsa et al., 2014). Accordingly, the reported 2D culture should not be used for high-performance drug screening (Braam et al., 2010; Guo et al., 2011; Matsa et al., 2011; Harris et al., 2013; Liang et al., 2013; Navarrete et al., 2013). More recent studies have been based on 3D CM tissue construction, showing improved maturation with respect to the 2D control (Huebsch et al., 2016; Jackman et al., 2016; Mannhardt et al., 2016; Schwan et al., 2016). In parallel, myocardial regeneration for repairing injured heart has progressed by using cell injections (Shiba et al., 2012, 2016), cell sheets (Masumoto et al., 2012; Kawamura et al., 2013), or cell patches (Menasché et al., 2015). However, the above *in vivo* studies were mostly based on poorly organized hPSC-CMs (Shao et al., 2015; Mathur et al., 2016), and only a few recent investigations have paid attention to the 3D cellular organization in engineered tissues, showing a longer-term survival (Riegler et al., 2015) and improved ventricular functions (Weinberger et al., 2016) after tissue engraftment.

To reproduce the *in vivo* cardiac tissue organization, nanofibers with high surface area to volume ratios were used for cardiac tissue engineering (Zong et al., 2005; Orlova et al., 2011; Hsiao et al., 2013; Joanne et al., 2016). CMs on the aligned nanofibers can form, for example, cell-elongated tissue-like constructs with enhanced maturation (Han et al., 2016; Xu et al., 2017) and improved ability to repair myocardial infarction (MI) (Lin et al., 2014). Critical issues such as limited cell infiltration in the nanofiber systems (Zong et al., 2005; Yu et al., 2014), fiber layer thickness, fiber degradability, and fiber stiffness remain to be addressed since they are important for the implantation and treatment of sustained re-entrant arrhythmias (Bursac et al., 2007) after transplantation.

In this work, we fabricated poly(lactic-co-glycolic acid) (PLGA), a biodegradable polymer approved by the US Food and Drug Administration, into aligned nanofibers with thickness 10- to 40-fold lower than previously reported (Kharaziha et al., 2014; Masoumi et al., 2014; Han et al., 2016; Joanne et al., 2016). Despite the low thickness, excellent operability of nanofibers could be obtained by fixing them on a silicone frame, which also enabled the establishment of floating cultures. 3D cardiac tissue-like constructs (CTLCs) were created by one-step seeding of high-purity CMs derived from hPSCs (Minami et al., 2012) on the aligned PLGA nanofibrous scaffold. The CMs within CTLCs infiltrated and enveloped the nanofiber sheets, showing elongation and high organization with upregulated expression of cardiac biomarkers and enhanced extracellular recording, which is beneficial especially for drug assessment. By engrafting CTLCs into the disconnected heart tissue created *in vitro* or scarred heart tissue with re-entrant arrhythmia, we also demonstrated the ability of CTLCs to rapidly couple with the host tissue, which resulted in the repair of the disconnected cardiac tissue and the suppression of re-entrant arrhythmias within the scarred region. Furthermore, the *in vivo* transplantation of CTLCs in an MI model showed excellent CM survival and cardiac functional improvement 4 weeks post surgery. Thus, CTLCs demonstrated their potential for clinical use in the future.

RESULTS

Cardiac Tissue-like Constructs Were Formed on Aligned Nanofibers

The aligned PLGA nanofibers (ANFs) were used as a culture scaffold to guide the growth and tissue formation of hiPSC-CMs, because they resembled native extracellular matrix (ECM) (Figure 1 and Figure S1) when compared with randomly arranged PLGA nanofibers (RNFs) (Figure S1A) and gelatin-coated flat substrates (Flat) used as control. To mimic collagen fiber bundles in muscle tissue (Gillies and Lieber, 2011) and produce the ECM-like pattern for engineered cardiac tissue (Kim et al., 2010), the diameter of the PLGA nanofibers was set at 500–2,000 nm (Figures S1B and S1C) and the thickness at 1.5–12 μm by varying the spinning time (Figures S1D and S1E). Despite the low thickness of the nanofiber sheets, ANFs demonstrated considerable flexibility (Movie S1) and anisotropic properties, which were evident not only in the structure but also in Young's modulus and wettability (Figures S1F–S1I).

Then, hiPSC-derived CMs were cultured on the prepared substrates for 14 days. The samples were then examined by electron microscopy (Figures 1E, 1H, 1I, S2A, and S2B) and tomography (Figures 1F and 1G, Movies S2 and S3). Interestingly, CMs could infiltrate and envelop both ANFs and RNFs because of the low thickness of nanofiber sheets (Figures 1F–1I and S1E), and the poly-dimethylsiloxane (PDMS) frame can enable the floating culture of CMs, which are both advantageous compared with methods using 2D topographically aligned cues. The alignment of large sarcomeric bundles could be observed only on ANFs, while randomly distributed bundles were seen on RNFs and Flat, indicating more mature sarcomeric organization of CMs on ANFs than the other two samples (Figures 1I, S2A, and S2B). Furthermore, dense CM sheets with various thicknesses ranging from 36 ± 5 μm (n = 3) to 160 ± 13 μm (n = 3) could be obtained by simply changing the number of seeded cells (Figures 1J–1M), which remained fully viable for 6 days after seeding (Figures S2C and S2D). By increasing the cell number or overlaying multiple CM sheets, higher tissue thickness could be achieved for transplantation. Because CM sheets on ANFs reproduced the *in vivo* arrangement, as demonstrated by their highly defined 3D anisotropic structure, we designated them as CTLCs.

Cardiomyocytes Demonstrated Improved Maturation within Cardiac Tissue-like Constructs

CTLCs were further analyzed by flow cytometry, immunostaining, and qPCR. Flow cytometry analysis indicated that before seeding, troponin T2 (cTnT)-positive CMs (253G1) constituted 91.16% ± 4.96% (n = 32) of the total cell population (Figures S2E and S2F). After 14 days of culture, the proportions of cTnT-positive CMs on ANFs and RNFs are 86.79% ± 5.1% (n = 3) and 85.85% ± 9.11% (n = 3) respectively, while that on Flat decreased dramatically to 71.101% ± 7.65% (n = 3) (Figure S2F), suggesting that other cells outgrew CMs on flat substrates with no topographical cue (Van Kooten et al., 1998). Moreover, immunostaining for cardiac tissue-specific markers revealed significantly higher expression of β-MHC, a cardiac maturity marker correlated with contractile velocity (Nakao et al., 1997), on ANFs than on Flat (Figure 2A). α-Actinin-positive sarcomeres and cTnT-positive myofilaments were well defined and positioned along ANFs, while a different arrangement was observed on RNFs and Flat (Figures 2A, 2B, and S2G). The analysis of mRNA expression revealed that several genes were upregulated in CMs cultured on ANFs compared with those cultured on other substrates (Figure 2C), including the genes involved in sarcomere structures (*ACTN2*, *TNNT2*, and *TNNI3*), cardiac maturation (*MYH7*), ventricular structures (*MYL2*, *HAND2*), and ER-Ca^{2+} function (*PLN* and *RYR2*). These findings were supported by hierarchical clustering analysis, which revealed that the expression profile of CTLCs was distinct from those of RNF- or Flat-grown cultures, in accordance with their differences in sarcomeric organization revealed by electron microscopy data (Figures 1I, S2A, and S2B).

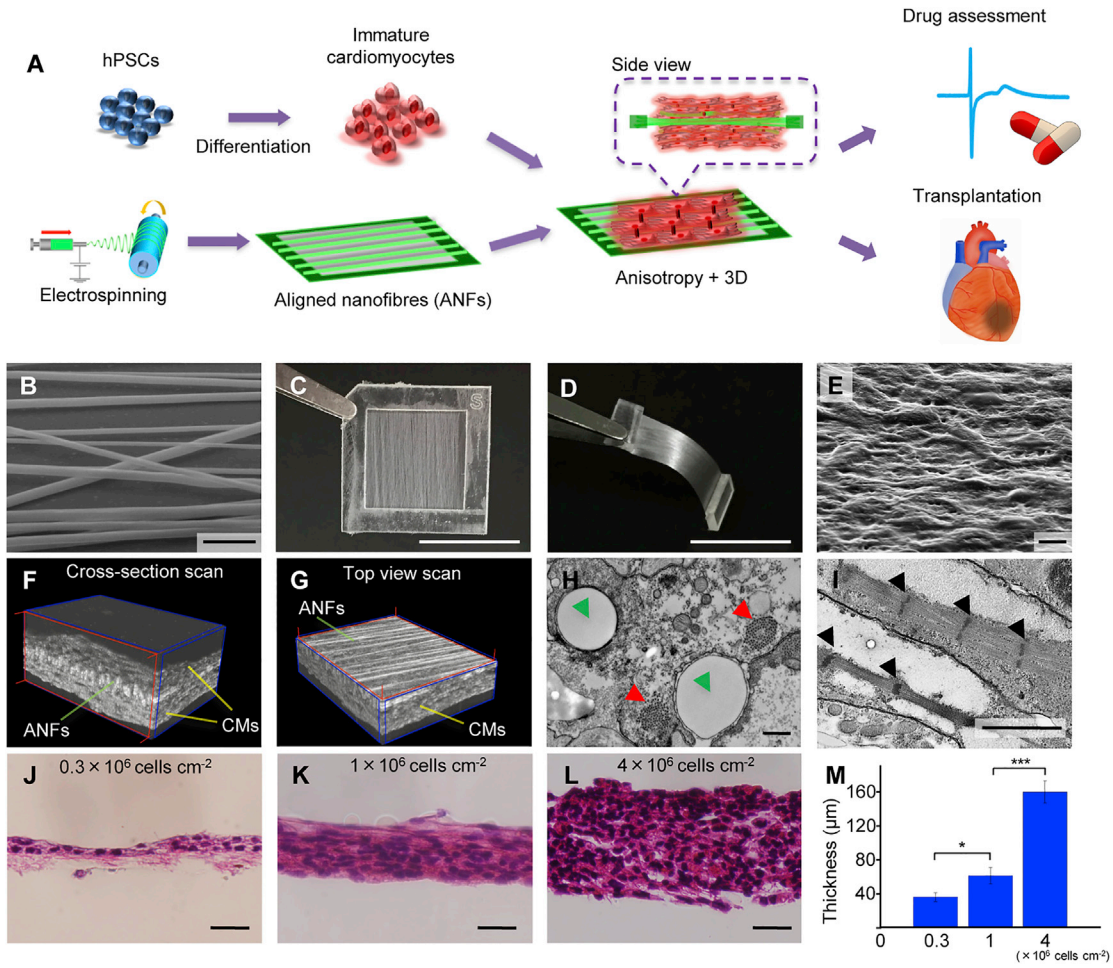

Figure 1. Cardiac Tissue-like Constructs Formed on Aligned Nanofibers

(A) Schematic representation of the experimental approach.

(B) Scanning electron microscopy (SEM) image of aligned nanofibers (ANFs). Scale bar, 5 μm.

(C) Image of the ANFs transferred to a poly-dimethylsiloxane (PDMS) frame. Scale bar, 1 cm.

(D) Cross-section of the PDMS frame with ANFs after being cut in the middle. Scale bar, 1 cm.

(E) SEM image of cardiomyocytes (CMs) 14 days after seeding on ANFs. Scale bar, 10 μm.

(F and G) Tomography images of CTLCs obtained by cross-section scan (F) and top view scan (G). For more details, see Movies S2 and S3.

(H and I) Transmission electron microscopy images of CMs on ANFs. The green, red, and black arrows indicate the cross-section of nanofibers, sarcomeric bundles, and Z bands in the actin-myosin system. Scale bars, 0.5 μm (H) and 2 μm (I).

(J–L) Histology of CTLCs with different cell seeding density: (J) 0.3 × 10^6 cells cm^{-2}; (K) 1 × 10^6 cells cm^{-2}; (L) 4 × 10^6 cells cm^{-2}.The tissue cut was along the ANF alignment. Scale bar, 50 μm.

(M) Thickness of CTLCs with different cell density. Data are represented as means ±SD, n = 3 independent experiments. *$p < 0.05$, ***$p < 0.001$ by one-way ANOVA followed by Tukey's post hoc test. See also Figures S1 and S2.

Cardiac Tissue-like Constructs Showed Increased Electrical Activity and Drug Response Compared with Conventional 2D Cultures

Since CMs are contractile cells responsive to electrical impulses, extracellular recording of spontaneous/stimulated electrical activity in contracting CMs can provide assessment of their functional integrity. Therefore, we compared the electrical characteristics of CMs cultured on high-density ANFs (H-ANFs), low-density ANFs (L-ANFs), RNFs, and Flat (Figure 3 and Figure S3). The larger amplitude of field potential (FP) observed for CMs plated on ANFs and RNFs compared with those grown on Flat indicated better cell attachment to nanofibers (Figures 3B, 3C, and 3E). FP amplitude was lower for the H-ANF than for the L-ANF samples; this was probably due to a thicker fiber layer, which reduced the degree of contact between CMs and electrodes, augmenting resistance. The amplitude was increased from day 2 after cell

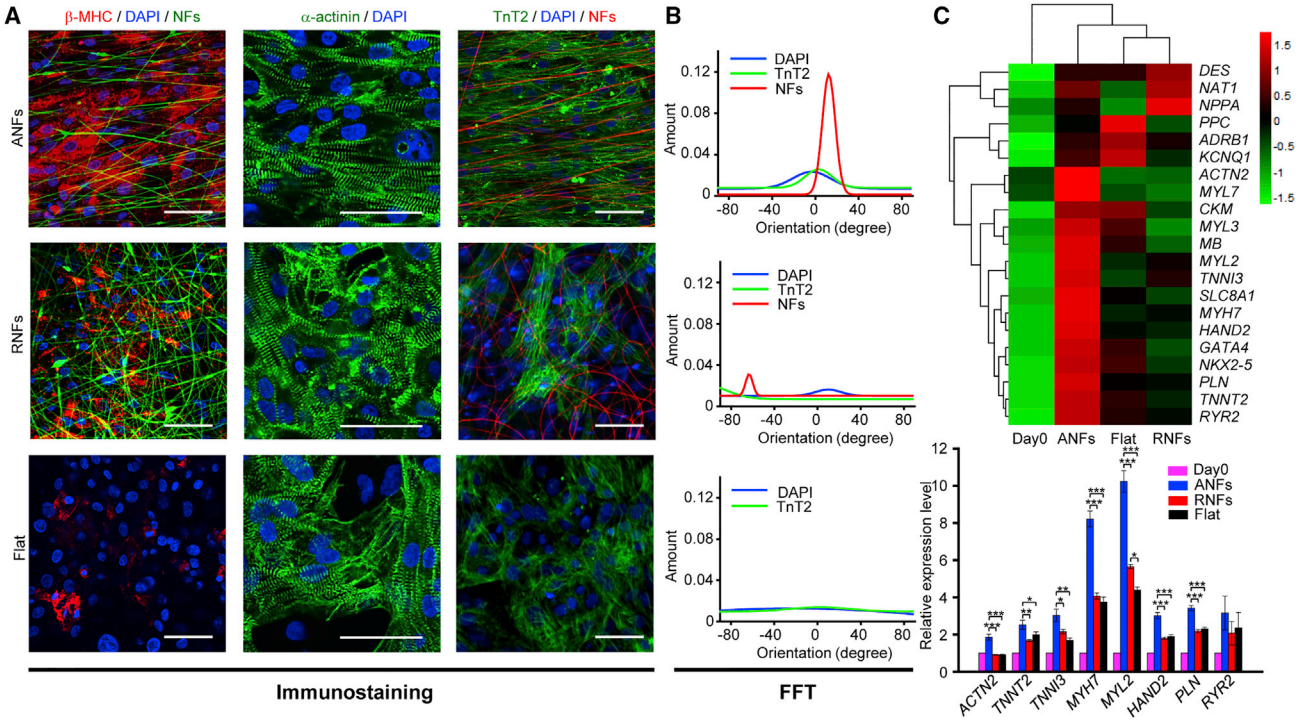

Figure 2. Enhanced Maturation of Cardiac Tissue-like Constructs

(A) Immunostaining images of β-MHC (red), and α-actinin and cTnT (green). Cardiomyocytes (CMs) were cultured on different substrates: aligned nanofibers (ANFs), random nanofibers (RNFs), and gelatin-coated flat substrate (Flat); nanofibers were fabricated with green or red dyes added before cell seeding. Scale bar, 50 μm.

(B) Fourier component analysis (FFT) of nuclei, nanofibers, and cTnT-positive thin filaments according to the positioning density on ANFs (upper panel), RNFs (middle panel), and Flat (bottom panel).

(C) qPCR analysis of gene expression in CMs, relative to day 0: *ACTN2* (α-actinin), *TNNT2* (cTnT), *TNNI3* (troponin I), *MYH7* (myosin heavy chain beta, β-MHC), *MYL2* (ventricular myosin light chain-2), *HAND2* (heart- and neural crest derivative-expressed protein 2), *PLN* (phospholamban), and *RYR2* (ryanodine receptor 2). The CMs were cultured for 14 days. Heatmap of *Z* score values shows genes expressed in different groups. The FPKM (fragments per kilobase of exon per million fragments mapped) value of each gene is normalized using Z scores. Data are represented as means ±SD, n = 3 independent experiments. *p < 0.05, **p < 0.01, and ***p < 0.001 by one-way ANOVA followed by Tukey's post hoc test.

See also Figure S2.

seeding and reached a plateau between days 6 and 10, indicating the developmental increase in the number of electrically active, synchronized cardiac cells (Banach et al., 2003).

Moreover, elliptical isochrones in the activation map of the H-ANF and L-ANF samples indicated anisotropic propagation of the electrical signal due to the direction-specific orientation of CMs (Figure 3D). Notably, electrical propagation in the Flat sample started from a site other than the stimuli site, suggesting weak attachment to electrodes and low homogeneity of CMs (Figure S3D), which also occasionally showed poor intercellular connectivity and coupling (Figure S3E).

In our experiments, CMs on the Flat samples detached from the electrodes after about 14 days because of poorer cell attachment and homogeneity, which led to a lower ratio of T-wave-detecting channels in the microelectrode array (MEA) (Figure 3F). However, CMs on thicker nanofibers (H-ANFs) demonstrated a higher ratio of recorded channels and long-term (over 32 days) monitoring of CTLCs, which is important for testing chronic drug effects on CMs (Figure S4A).

The potential arrhythmia liability of a drug is required to be assessed during cardiovascular drug screening and toxicity testing. To evaluate drug effects on the electrophysiological properties of CTLCs, E4031, a specific blocker of the rapid component of the delayed rectifier potassium current (I_{Kr}), was applied to different CM cultures, which were then analyzed for QT interval duration, used as an indicator of electric depolarization/repolarization of CMs. Significant QT interval prolongation was observed for all three samples after E4031 treatment

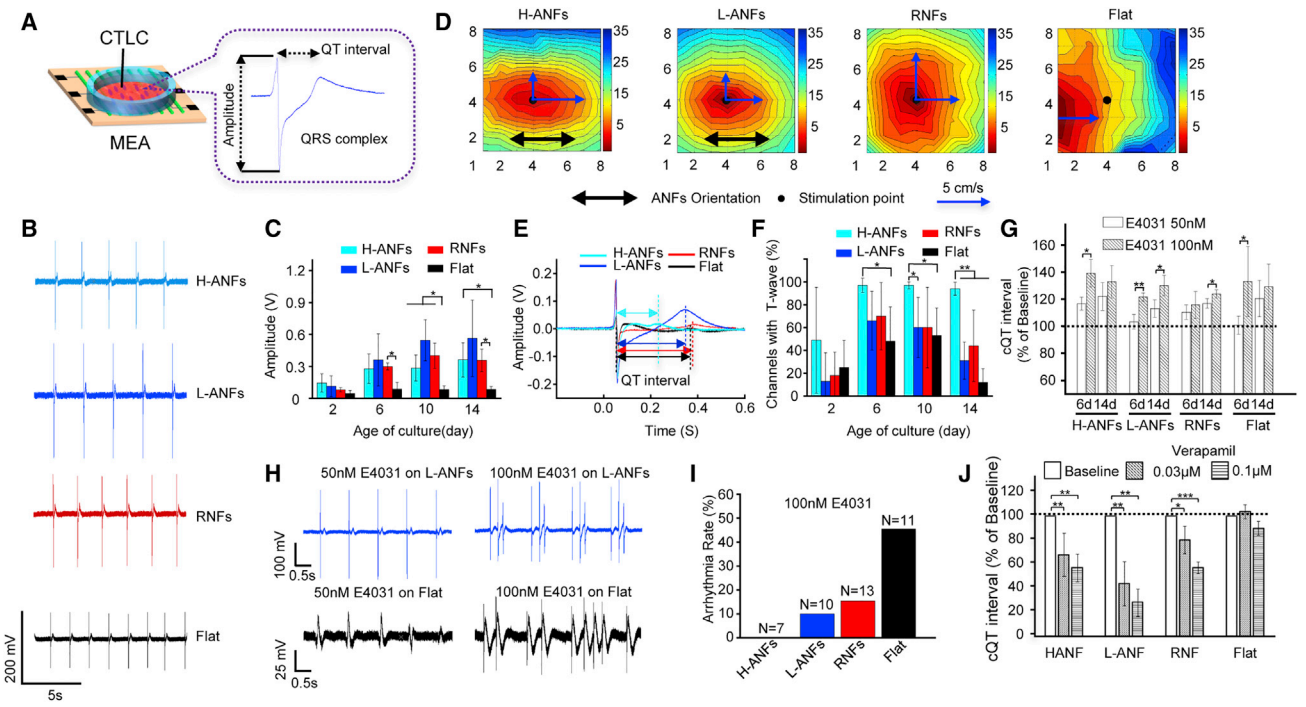

Figure 3. Cardiac Tissue-like Constructs for More Appropriate Drug Assessment Compared with the 2D Flat Group

(A) Schematic representation of CTLCs on the microelectrode array (MEA) and a representative electrogram of the field potential (FP) recorded from CMs illustrating the analyzed parameters.

(B) Spontaneous beatings of cardiomyocytes (CMs) on day 6 after seeding.

(C) Amplitude of CM field potential (FP) at different culture times (n = 4–5 independent biological replicates).

(D) Activation maps showing the propagation of stimulated contractility on day 6. The blue arrow demonstrates the propagation velocity.

(E) Overlapped FPs of CMs cultured on different substrates on day 6; colored arrows mark the QT intervals of different samples.

(F) Percentage of channels that recorded a T wave (n = 6–10 independent biological replicates).

(G) E4031 effects on corrected QT intervals of CMs (n = 3–5 independent biological replicates).

(H) Arrhythmia occurring after E4031 application on day 14.

(I) The ratio of samples with arrhythmia after E4031 application (100 nM) on day 14.

(J) Verapamil effects on corrected QT intervals of CMs (n = 3–5 independent biological replicates). Data are represented as means ±SD. For (C), (F), and (J), *p < 0.05, **p < 0.01, and ***p < 0.001 by one-way ANOVA followed by Tukey's post hoc test. For (G), *p < 0.05, **p < 0.01 by Student's t test. Abbreviations: L-ANFs and H-ANFs, low-density and high-density aligned nanofibers, respectively; RNFs, random nanofibers; Flat, gelatin-coated flat substrate. See also Figures S3–S5.

(Figures 3G and S4B); however, the drug effects on Flat-cultured CMs showed higher variability compared with those observed in nanofiber-cultured CMs (Figure 3G). In addition, E4031 caused more significant manifestations of arrhythmia in the Flat-cultured than in the nanofiber-cultured CMs (Figures 3H and 3I). Lower QT interval variability and less significant arrhythmic activity suggested higher electrophysiological homogeneity of CMs cultured on the nanofibers compared with those grown on Flat. The analysis of CM chronotropic responses to isoproterenol and propranolol indicated that the former increased the beat rate, while the latter blocked the stimulatory effect in all samples (Figures S4C and S4D). In addition, 0.03 μM Ca^{2+} channel blocker verapamil could lead to significant shortening of the QT interval in all the nanofiber samples but not in Flat samples (Figures 3J and S5A). All four samples demonstrated a similar drug response after the addition of the sodium channel inhibitor quinidine (Figures S5B and S5C). Overall, these data indicate that the CTLC faithfully reproduced the *in vivo* structural and functional properties of cardiac tissue and is, therefore, a better model for drug cardiotoxicity testing than conventional 2D CM cultures.

Cardiac Tissue-like Construct Engraftment Resulted in Synchronization of Disconnected CM Tissue and Suppression of the Re-entrant Spiral Wave

We next performed *in vitro* engraftment experiments to characterize the ability of CTLCs to establish contacts and couple with the host CM sheets. Two CTLCs engrafted

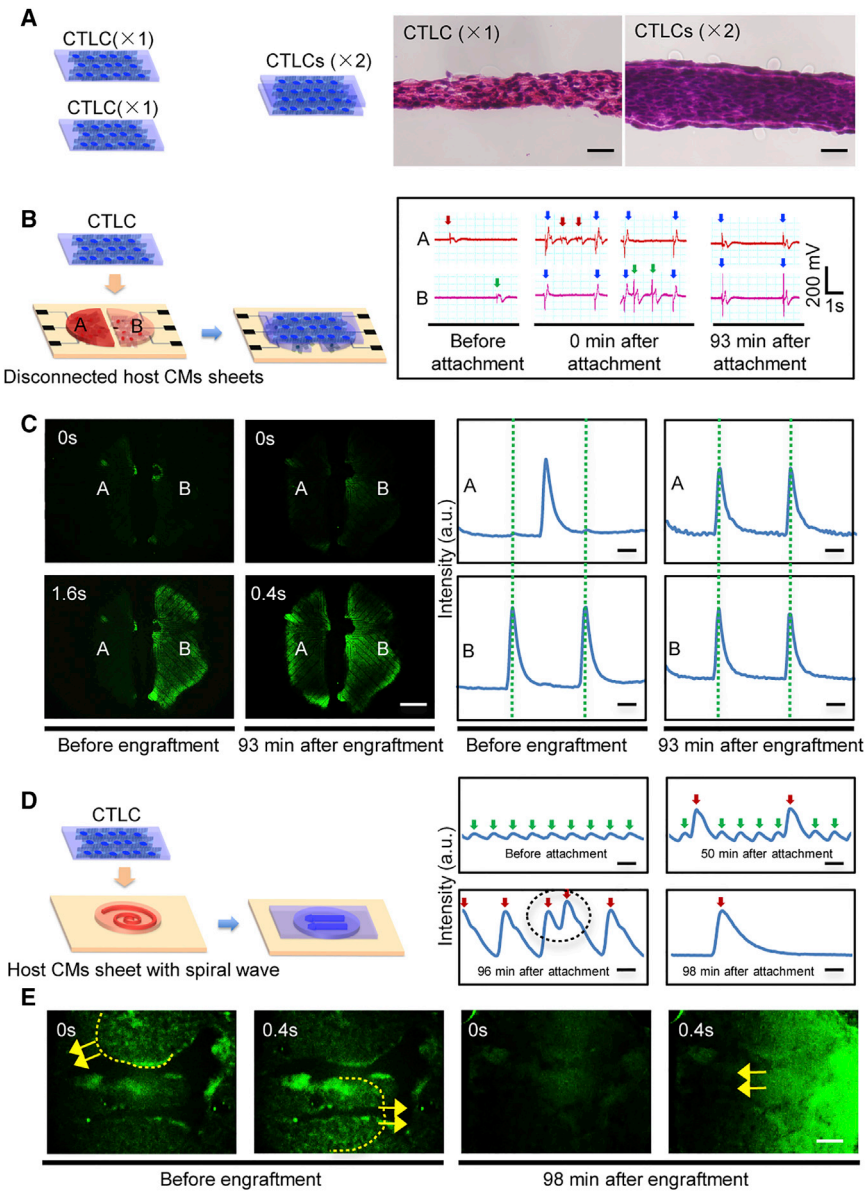

Figure 4. Cardiac Tissue-like Constructs Can Synchronize Disconnected Cardiomyocyte Tissues and Suppress Re-entrant Arrhythmia within Scarred Cardiomyocyte Sheets

(A) *In vitro* engraftment of two CTLC samples. Histological section images show a single CTLC (×1) and two engrafted CTLCs (×2; 3 days after engraftment). Scale bar, 50 μm.

(B) Engraftment of a CTLC on two disconnected sheets of GCaMP3-positive host cardiomyocytes (CMs) on the microelectrode array (MEA) and recorded field potential before and after engraftment. The arrows mark the beating of the left host CM sheet (red, recorded by electrode A), right host CM sheet (green, recorded by electrode B), and the CTLC (blue).

(C) Fluorescence images (left) and Ca^{2+} transients (right) of the two GCaMP3-positive (calcium sensor) host CM sheets before and after CTLC engraftment. Complete coupling was achieved at 81 ± 49 min (means ± SD, n = 3 independent biological replicates). For more details, see Movie S4. Scale bar, 1 mm.

(D) Engraftment of the GCaMP3-positive CTLC on a GCaMP3-positive host CM sheet with spiral waves. Green and red arrows indicate oscillations of the host CM sheet and CTLC, respectively. The black circle marks fast beating of the CTLC. Scale bar, 1 s.

(E) A spiral wave (dashed line) is created in the scarred host CM sheet. The yellow arrow marks the propagation direction of GCaMP3 fluorescence. For more details, see Movie S6. Scale bar, 1 mm.

See also Figure S6.

together for 3 days were examined by histology, which demonstrated the absence of a clear boundary between the two samples and showed that the engrafted tissue was 2-fold thicker than a single CTLC layer (Figure 4A), indicating rapid integration of the two CTLC samples. Moreover, a CTLC placed over two independently beating host CM sheets separated by a barrier was able to synchronize their contraction 81 ± 49 min (n = 3) after attachment (Table 1), as indicated by the electrical signal of the MEA and calcium sensor fluorescence protein GCaMP3 (Figures 4B and 4C and Movie S4). As a control test, the CMs were also cultured on RNFs and placed on two independent host CM sheets (Movie S5). Similarly, the CM sheets were synchronized at 73.3 ± 18 min (n = 3) after attachment (Table 1). These results indicate that the CTLC could integrate with the host CM sheets and help establish rapid electrical coupling between disconnected areas in the heart, suggesting potential for CTLCs to heal re-entrant cardiac arrhythmias. To test this hypothesis, spiral waves were induced in the GCaMP3-positive scarred cardiac host CM sheet (Figures 4D and 4E and Movie S6) to model re-entrant tachyarrhythmia (Kadota et al., 2013). Shortly after CTLC attachment to the scarred tissue, we recorded two sets of calcium signals: strong and relatively slow signals conducted from the CTLC, and weak and fast re-entrant signals or spiral wave of the host CM sheet. Slow acceleration of CTLC

Table 1. Summary of Time for Cardiac Tissue-like Constructs to Couple with Disconnected Tissues or Terminate the Spiral Wave in Scarred Tissues

Coupling Time for CTLCs on Disconnected Tissues		Time for CTLCs to Terminate Spiral Wave in Scarred Tissues	
ANF (n = 3 independent biological replicates)	RNF (n = 3 independent biological replicates)	ANF (n = 4 independent biological replicates)	RNF
81 ± 49 min	73.3 ± 18 min	129.5 ± 34 min	NA

beating was due to the gradual coupling with the host CM sheet, which was finally achieved at 129.5 ± 34 min (n = 4) (Table 1 and Figure S6). Due to the coupling, the scar area, where the propagating spiral wave was pinned, was overlaid, and the spiral wave was able to propagate over rather than around the scar, leading to unpinning and then termination of the spiral waves. We further applied electrical stimulation to induce a spiral wave in a scarred host CM sheet with various engraftment (acellular nanofiber sheet and CTLC) (Movie S7), finding that the spiral wave can only be induced in the acellular nanofiber sheet group but not in the CTLC group. The data suggested that CTLC could effectively prevent the recurrence of spiral wave. Moreover, the control test with an RNF-CM sheet could not terminate the spiral wave at 12 hr after attachment (Movie S6), indicating that the aligned structure of CMs may play a role in suppressing the arrhythmia, and CTLCs have higher potential to alleviate cardiac arrhythmia.

Cardiac Tissue-like Constructs Integrated with the Epicardium Improved the Function of the Infarcted Heart

We analyzed and optimized the parameters for CTLC transplantation (Figures S7A and S7B). CTLCs with 5–8 × 10^6 CMs were transplanted to the epicardium of the normal nude rat ventricle for 2 weeks (Figure S7C), showing no histological gaps (Figure 5A). The CTLC was monitored by immunostaining for human TnT (hTnT), which was expressed in the transplanted CTLC but not in the recipient rat heart (Figure 5B). Distinct thick clusters (390 ± 36 μm, n = 3) of transplanted hTnT-positive CMs (96.6% ± 1.2% of total cells [n = 3]; Figure S7D) were observed in the rat hearts, while some hTnT-positive cells infiltrated the epicardium of the rat ventricle (Figure 5B). In addition, the alignment of CMs and organized compact sarcomeric structures (Figures 5B and S7D) could be observed within transplanted CTLC grafts. These results indicate the efficient transplantation of CTLCs and the survival of hiPSC-derived CMs for 14 days post transplantation.

Furthermore, CTLCs were delivered to the hearts of 12 rats with MI (Figures 5C and 5D); 17 MI rats received acellular nanofiber scaffolds as controls (Figure 5E). The implanted CTLCs were visible on the surface of the rat heart at week 4 after transplantation (Figures 5C and 5D); in contrast, acellular nanofiber scaffolds were hardly detectable (Figure 5E).

We also investigated the small blood vessels by using CD31 immunostaining. The density of small vessels was higher in the CTLC group than in the control group (Figures 6A–6C). The baseline ejection fraction at week 0 did not differ significantly between the two groups ($p = 0.41$); however, there was an increase in the ejection fraction in rats treated with CTLCs at week 4 after transplantation compared with week 0 (50.63% ± 6.41%, n = 12, versus 37.50% ± 5.15%, n = 17, respectively), while the ejection fraction in the control samples did not change during the experiment (Figure 6D). The ejection fraction values at 4 weeks after treatment was significantly different between the two groups ($p < 0.001$). Moreover, transplantation with CTLC also improved the fractional shortening ($p < 0.001$) and left ventricular end-systolic diameter (LVESD) ($p < 0.05$) (Figures 6E and 6F). The left ventricular end-diastolic diameter (LVEDD) demonstrated a significant increase in the control group ($p < 0.05$) but not in the CTLC group over 4 weeks ($p = 0.95$) (Figure 6G). CD68 immunostaining indicated that there were no obvious inflammatory reactions in both groups at 4 weeks after transplantation (Figures S7E and S7F). These results clearly demonstrated functional improvement in the MI heart provided by CTLCs due to the transplantation of functional well-organized CMs.

DISCUSSION

Cell therapy based on hPSC-derived CMs is a promising approach for cardiac regeneration (Georgiadis et al., 2014). Currently, efficient production of robust hPSC-CMs is possible in serum-free conditions (Kattman et al., 2011; Minami et al., 2012). However, the hPSC-CMs obtained in 2D cultures morphologically and functionally resemble immature CMs (Yang et al., 2014), as demonstrated by their random sarcomere structure and distribution of the nuclei, lower expression of heart-specific genes, decreased contractile force, and electrophysiological characteristics different from those of adult CMs (Robertson et al., 2013; Yang et al., 2014). These differences could affect the functional properties and drug responses of hPSC-CMs.

The problem could be solved by creating a nature-mimicking environment, which would provide the appropriate biochemical and structural cues for CM maturation. In this study, we used hPSC-derived CMs aligned on biodegradable PLGA nanofibers to generate tissue constructs

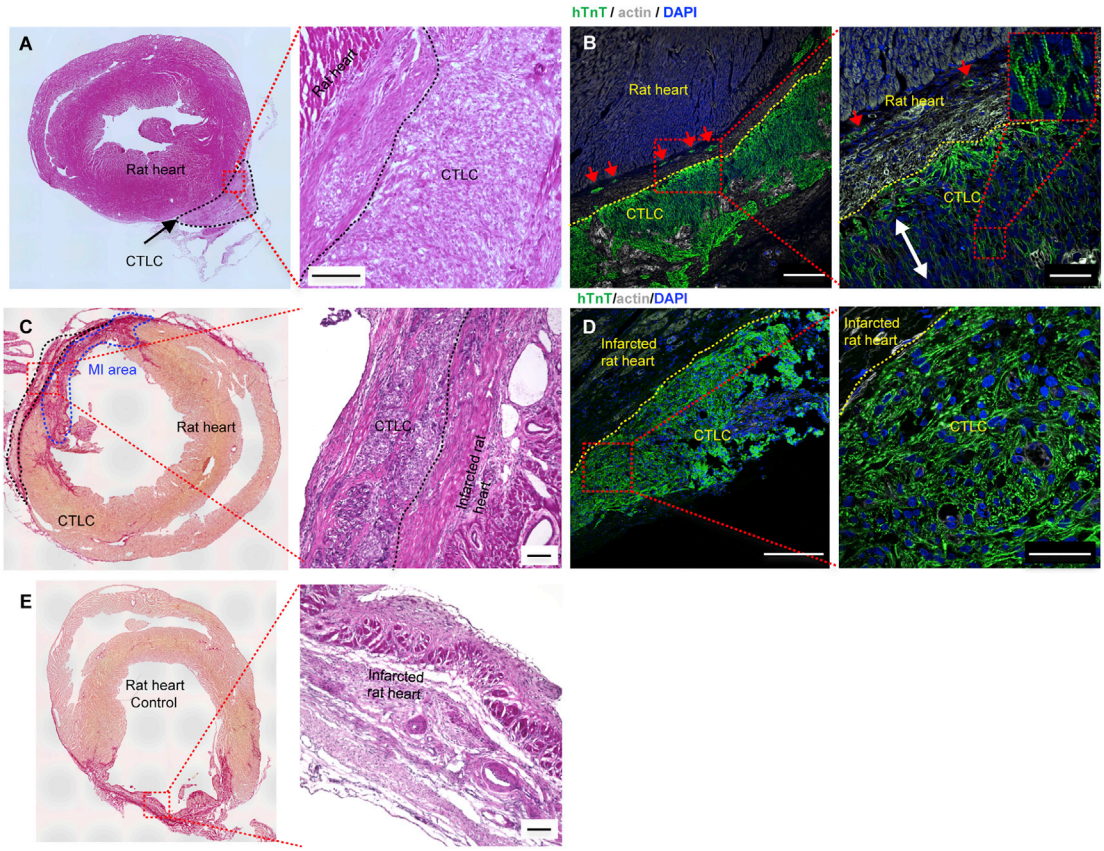

Figure 5. Cardiac Tissue-like Constructs Integrated with the Epicardium

(A–D) Histological sections of CTLCs after being transplanted on the rat heart without (A and B) or with myocardial infarction (MI) (C and D). (A) and (B) were obtained at 2 weeks and (C) and (D) 4 weeks after transplantation. Scale bars in (A) and (C), 100 μm. (B and D) Double immunostaining of consecutive sections of CTLCs after being transplanted on the rat heart without (B) or with (D) MI for hTnT (green) and actin (white); nuclei were stained with DAPI (blue). The dashed line marks the CTLC boundary. The red arrows indicate that hTnT-positive cardiomyocytes (CMs) infiltrated the epicardium of the rat ventricle. The white arrow indicates the alignment of CMs. Scale bars in (B) and (D), 200 μm (left panel), 50 μm (right panel).

(E) Histological sections of MI heart with acellular nanofiber as control. Scale bars, 100 μm.

See also Figure S7.

with morphological properties similar to those of the myocardium (Kim et al., 2010), and avoided immunogenic potential or ethical conflict compared with those methods using decellularized myocardial slices (Schwan et al., 2016). We also demonstrated that ANFs enhanced anisotropy and 3D formation of CMs compared with RNFs and Flat samples. Importantly, because of the low thickness of the nanofiber sheets, CMs easily infiltrated and enveloped the nanofibers.

Although compared with previous reports regarding CM maturation, such as biowire (Nunes et al., 2013), nanopattern (Pioner et al., 2016), dynamic culture (Jackman et al., 2016), and engineered heart tissue (Mannhardt et al., 2016), CTLCs, without any external physical stimulation, do not show a higher maturation level of CMs, however, their versatility and handy operability allows flexible applications in both drug assessment and transplantation. Furthermore, additional measures such as electrical/mechanical stimulation may be applied to further promote CM maturation in CTLCs. Therefore, CLCTs could be an important complement to present technologies.

We also demonstrated the potential of CTLCs in drug screening. Previous single-cell- or cluster-based models have shown heart-specific functional properties (Zwi et al., 2009; Ma et al., 2011; Matsa et al., 2011); however, single cells or small cell clusters do not reproduce the functional activity of well-organized multicellular networks existing in the heart and cannot serve as accurate models to assess complex cardiac phenomena such as arrhythmia (Kadota et al., 2013). The CTLC-MEA system offers a promising model for *in vitro* tissue-based drug screening as it presents a 3D environment to promote the alignment,

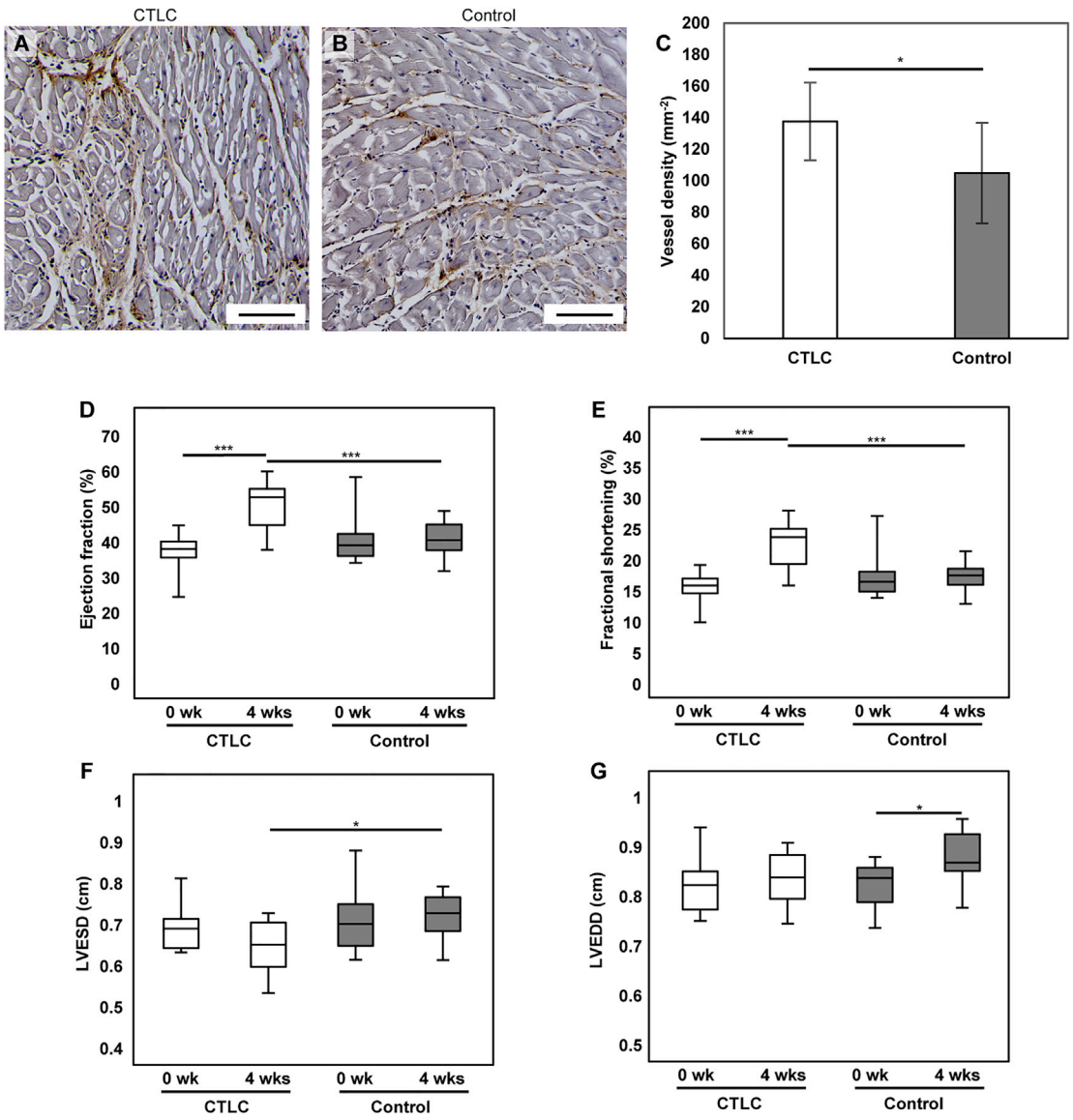

Figure 6. Cardiac Tissue-like Constructs Improved the Function of the Infarcted Heart

(A and B) Capillary formation at the peri-ischemic zone in MI heart 4 weeks after transplantation of CTLCs (A) or acellular control (B). The sections are immunostained with CD31. Scale bars, 100 μm.

(C) Quantification of the density of CD31-positive capillaries. Data are represented as means ± SD. CTLC, n = 7 rats; control, n = 6 rats. *p < 0.05 by Student's t test.

(D–G) Change of ejection fraction (D), fractional shortening (E), left ventricular end-systolic diameter (LVESD; F), and left ventricular end-diastolic diameter (LVEDD; G) of infarct rat heart following CTLC transplantation versus the control group at 0 weeks and 4 weeks after transplantation. Data are represented as means ± SD. CTLC, n = 12 rats; control, n = 17 rats. *p < 0.05 and ***p < 0.001 by one-way ANOVA followed by Tukey's post hoc test.

See also Figure S7.

structural organization, and maturation of CMs, thus mimicking the *in vivo* myocardium. The CTLC showed an excellent response to the applied drugs (E4031, isoproterenol, verapamil, and quinidine) and demonstrated decreased arrhythmia compared with the Flat sample at the same E4031 concentration. In addition, since hPSC-CMs mature within 35 days (Snir et al., 2003), stable and robust long-term CTLCs on the MEA chip could be constantly monitored for CM maturation. Using other biocompatible and nondegradable materials such as

polymethylglutarimide (PMGI) for nanofiber fabrication (Li et al., 2016), the CTLC-MEA system could sustain CM cultures over several months, which is the time required for CM maturation according to a previous study (Kamakura et al., 2012). In short, the CTLC has proved to be an accurate and robust model for screening drugs designed for cardiovascular diseases.

We confirmed rapid electrical integration between the CTLC and the host tissue by an *in vitro* test. The complete coupling time (81 ± 49 min) was 2-fold higher than that for rat CM tissue (Haraguchi et al., 2006), probably because of considerable differences in the expression of key ion channels, beating rates, and myofilament composition between rat and human CMs (Karakikes et al., 2015). In addition, we reported that the coupling of tissue grafts could unpin spiral waves in the infarcted cardiac tissue, which previously could be achieved only by harmful electrical stimulation (Tanaka et al., 2009; Feng et al., 2014). The CTLC may be useful as an *in vitro* model for the study of hPSC-CM engraftment and integration, thus providing information for preclinical tests in humans.

Moreover, the CTLC demonstrated sufficient degradability, operability, and robustness (Movie S1 and Figures S7B, S7C, S7G, and S7H). Despite the high Young's modulus of PLGA nanofibers (Figure S1H), the nanofiber sheets in this study had relatively low thickness (~12 μm), which is 10- to 40-fold lower than those in previous reports (Kharaziha et al., 2014; Masoumi et al., 2014; Joanne et al., 2016) and may present an advantage by reducing the risk of re-entrant arrhythmias (Bursac et al., 2007) and inflammatory reactions. In addition, the CTLC with high thickness (~400 μm) integrated with the host MI hearts and then improved their function 4 weeks after transplantation, which also proved that when taking together the degradability, low thickness of the fiber sheet, and the high thickness of CMs, the stiffness of PLGA may not be a major issue for transplantation. These features together with the highly anisotropic and dense organization of CMs as well as the practical versatility make CTLCs clearly advantageous over previous transplantation with a CM-seeded nanofibrous scaffold (Lin et al., 2014; Joanne et al., 2016). Compared with the state-of-the-art temperature-responsive cell sheet technique (Masumoto et al., 2012; Kawamura et al., 2013), the one-step preparation and its one-step delivery of high-thickness CMs sheet may make the CTLC an important complement and alternative option.

Despite the improvement shown by CTLCs in regard to both drug response and MI regeneration, it is still too early to claim that the CTLC can be successfully used in drug screening and regenerative medicine, since our data are obtained based on transplantation in an MI rat model and a limited number of drug types. In the future, a more systematic drug screening should be performed to further verify the robustness of CTLCs. Transplantations using a clinically relevant large-animal model should be evaluated for long-term effects.

In conclusion, we created organized and functional CTLCs. Multilayered elongated CMs within the constructs showed upregulated gene expression of cardiac markers, enhanced extracellular recording, and robust drug response. When used for engraftment, CTLCs demonstrated excellent operability while enabling rapid coupling and suppression of re-entrant arrhythmia in disconnected or scarred tissue blocks. We also demonstrated post-surgery cell survival in CTLCs and their ability to repair MI in a rat model. Overall, the CTLCs have great potential for future use in cell-based applications, including drug testing and regenerative cardiac therapy.

EXPERIMENTAL PROCEDURES

Differentiation and Culture of hiPSC-Derived CMs

hiPSCs (253G1, 201B7 [as noted in the legend]) and GCaMP3-positive hiPSCs (253G1) were maintained or generated as previously reported (Hockemeyer et al., 2009; Shiba et al., 2012) and differentiated according to the published method (Minami et al., 2012). All experiments involving the use of hiPSCs were performed following the Kyoto University guidelines. After 1–2 months of differentiation, floating colonies of CMs were collected and dispersed into a single-cell suspension by stirring for 1–2 hr in protease solution: 0.1% collagenase type I, 0.25% trypsin, 1 U/mL DNase I, 116 mM NaCl, 20 mM HEPES, 12.5 mM NaH_2PO_4, 5.6 mM glucose, 5.4 mM KCl, and 0.8 mM $MgSO_4$ (pH 7.35). After dispersion, the cells were filtered through a 40-μm cell strainer (BD Falcon, USA) and re-suspended at a density of 1×10^6 cells cm^{-2} in serum-supplemented cardiac differentiation medium: IMDM (Sigma-Aldrich) with 20% fetal bovine serum (FBS; Gibco), 1% MEM nonessential amino acid solution (Sigma-Aldrich), 1% penicillin/streptomycin (Gibco), 2 mM L-glutamine (Sigma-Aldrich), 0.001% 2-mercaptoethanol (Gibco), and 0.005 N NaOH, with 10 ng/mL BMP_4 (R&D Systems), and plated on ANFs, RNFs, or 0.1% gelatin-coated flat substrates (Flat). The medium was changed to serum-free medium (cardiac differentiation medium without FBS) every 4 days starting from day 2.

In Vitro Engraftment

CTLCs were created by seeding regular or GCaMP3-positive CMs on H-ANFs at a density of 1×10^6 cells cm^{-2}. The RNF-CM sheets were created by seeding the same density of CMs on RNFs. The disconnected CM sheets were created by seeding GCaMP3-positive CMs at the same density on the substrate within a 5-mm PDMS ring, and sheets A and B were isolated by a 200-μm-wide PDMS barrier; the barrier was removed 2 days after seeding. Host CM sheets with spiral waves were prepared by seeding GCaMP3-CMs on gelatin-coated flat substrates at the same density and inflicting a 5-mm scar by abrasion; spiral waves were initiated by rapid pacing

(Isomura et al., 2008) at frequencies ranging from 2 to 4 Hz with a stimulus generator (Multi Channel Systems). The CTLCs were used for engraftment 5–6 days after seeding.

In Vivo Transplantation

Animal experiments were approved by the ethics committee of Osaka University and were performed following the committee's guidelines. For the transplantation test on normal heart, 8-week-old male nude rats (CLEA Japan, Japan) were used for transplantation. To create an MI model, thoracotomy was performed between the fourth and fifth intercostal spaces, and MI was induced by ligation of the left coronary artery, as described previously (Memon et al., 2005). HiPSC-CMs ($5–8 \times 10^6$ cells) were seeded on the H-ANFs in a 1×1 cm^2 PDMS frame for 1 day. Before transplantation, cells were treated with 5 mg cm^{-2} of Cellnest recombinant peptide based on human collagen type I (Fujifilm, Japan) at room temperature for 5 min; then, the PDMS frame was cut, and the CTLCs were placed on the epicardium and covered with Beriplast P (CSL Behring, USA). Echocardiography was performed using an ultrasound machine (SONOS 5500, Agilent Technologies) equipped with an annular array transducer operating at 12 MHz (Memon et al., 2005). The ejection fraction (EF) was calculated using the following formula: EF (%) = $(LVEDD^3 - LVESD^3)/LVEDD^3 \times 100$ (%). Rats without and with MI were killed at 14 days and 4 weeks post surgery, respectively, and the hearts were harvested and used to prepare 7-μm-thick cryosections for histology and immunostaining with an anti-TnT antibody (Abcam Plc) and phalloidin; cell nuclei were stained with DAPI (Life Technologies).

Statistical Analysis

All quantitative data are presented as the mean ± SD. The difference between two groups was analyzed by one-tailed Student's t test, and $p < 0.05$ was considered statistically significant. Comparison tests among multiple groups were analyzed by one-way ANOVA followed by Tukey's post hoc test, and $p < 0.05$ was considered statistically significant.

SUPPLEMENTAL INFORMATION

Supplemental Information includes Supplemental Experimental Procedures, seven figures, and seven movies and can be found with this article online at https://doi.org/10.1016/j.stemcr.2017.09.007.

AUTHOR CONTRIBUTIONS

J.L., L.L., and Y.C. conceived the project. J.L., I.M., M.S., N.N., Y. Sawa, Y.C., and L.L. designed the experiments. J.L., I.M., M.S., L.Y., S.Y., S.M., Y. Shiba, N.M., S.F., M.Y., S.L., J.Q., X.L., L.W., H.K., and L.L. performed experiments. All authors contributed to data analysis and interpretation. J.L., Y.C., and L.L. wrote the manuscript.

ACKNOWLEDGMENTS

We thank Dr. M. Hörning, K. Tsuji, Dr. K. Hasegawa, and Prof. T. Asada for helpful suggestions and discussions. We also thank Panasonic Co., Fujifilm Co., Tamai Kasei Co., Ltd., JMS Co., Ltd., and SAROUTE Co., Ltd. for their support with the analysis and cell transport. This work was supported by the Japan Society for the Promotion of Science (JSPS) Grants-in-Aid for Scientific Research (B) (15H03948, 26289065, 23310087, 26286027), Grants-in-Aid for Scientific Research (C) (15K08270), and Grants-in-Aid for JSPS Fellows (26.04046). The research is (partially) supported by the Japan Agency for Medical Research and Development (AMED) program, the European Commission (contract no. 604263 [Neuroscaffolds]), and the French National Research Agency (ANR; contract number ANR-12-RPIB-0015 [Cardiac Patch]). WPI-iCeMS was supported by the World Premier International Research Centre Initiative (WPI), MEXT, Japan. Kyoto University (J.L., I.M., N.N., Y.C., and L. L.) filed three provisional Japanese and one international patent applications based on the research presented here. N.N. is an employee and shareholder of Stem Cell & Device Laboratory, Inc., I.M. is a shareholder of Myoridge. Co. Ltd, Y.S.'s laboratory received funding from the TERUMO Company.

Received: January 27, 2017
Revised: September 11, 2017
Accepted: September 11, 2017
Published: October 26, 2017

REFERENCES

Banach, K., Halbach, M.D., Hu, P., Hescheler, J., and Egert, U. (2003). Development of electrical activity in cardiac myocyte aggregates derived from mouse embryonic stem cells. Am. J. Physiol. Heart Circ. Physiol. *53*, H2114–H2123.

Braam, S.R., Tertoolen, L., Van De Stolpe, A., Meyer, T., Passier, R., and Mummery, C.L. (2010). Prediction of drug-induced cardiotoxicity using human embryonic stem cell-derived cardiomyocytes. Stem Cell Res. *4*, 107–116.

Burridge, P.W., Matsa, E., Shukla, P., Lin, Z.C., Churko, J.M., Ebert, A.D., Lan, F., Diecke, S., Huber, B., and Mordwinkin, N.M. (2014). Chemically defined generation of human cardiomyocytes. Nat. Methods *11*, 855–860.

Bursac, N., Loo, Y., Leong, K., and Tung, L. (2007). Novel anisotropic engineered cardiac tissues: studies of electrical propagation. Biochem. Biophys. Res. Commun. *361*, 847–853.

Chong, J.J., Yang, X., Don, C.W., Minami, E., Liu, Y.-W., Weyers, J.J., Mahoney, W.M., Van Biber, B., Cook, S.M., Palpant, N.J., et al. (2014). Human embryonic-stem-cell-derived cardiomyocytes regenerate non-human primate hearts. Nature *510*, 273–277.

Feng, X., Gao, X., Pan, D.-B., Li, B.-W., and Zhang, H. (2014). Unpinning of rotating spiral waves in cardiac tissues by circularly polarized electric fields. Sci. Rep. *4*, 4831–4834.

Feric, N.T., and Radisic, M. (2016). Maturing human pluripotent stem cell-derived cardiomyocytes in human engineered cardiac tissues. Adv. Drug Deliv. Rev. *96*, 110–134.

Georgiadis, V., Knight, R.A., Jayasinghe, S.N., and Stephanou, A. (2014). Cardiac tissue engineering: renewing the arsenal for the battle against heart disease. Integr. Biol. (Camb) *6*, 111–126.

Gillies, A.R., and Lieber, R.L. (2011). Structure and function of the skeletal muscle extracellular matrix. Muscle Nerve *44*, 318–331.

Guo, L., Abrams, R., Babiarz, J.E., Cohen, J.D., Kameoka, S., Sanders, M.J., Chiao, E., and Kolaja, K.L. (2011). Estimating the risk of drug-induced proarrhythmia using human induced pluripotent stem cell derived cardiomyocytes. Toxicol. Sci. *12*, 281–289.

Han, J., Wu, Q., Xia, Y., Wagner, M.B., and Xu, C. (2016). Cell alignment induced by anisotropic electrospun fibrous scaffolds alone has limited effect on cardiomyocyte maturation. Stem Cell Res. *16*, 740–750.

Haraguchi, Y., Shimizu, T., Yamato, M., Kikuchi, A., and Okano, T. (2006). Electrical coupling of cardiomyocyte sheets occurs rapidly via functional gap junction formation. Biomaterials *27*, 4765–4774.

Harris, K., Aylott, M., Cui, Y., Louttit, J.B., Mcmahon, N.C., and Sridhar, A. (2013). Comparison of electrophysiological data from human-induced pluripotent stem cell–derived cardiomyocytes to functional preclinical safety assays. Toxicol. Sci. *134*, 412–426.

Hockemeyer, D., Soldner, F., Beard, C., Gao, Q., Mitalipova, M., Dekelver, R.C., Katibah, G.E., Amora, R., Boydston, E.A., Zeitler, B., et al. (2009). Efficient targeting of expressed and silent genes in human ESCs and iPSCs using zinc-finger nucleases. Nat. Biotechnol. *27*, 851–857.

Hsiao, C.W., Bai, M.Y., Chang, Y., Chung, M.F., Lee, T.Y., Wu, C.T., Maiti, B., Liao, Z.X., Li, R.K., and Sung, H.W. (2013). Electrical coupling of isolated cardiomyocyte clusters grown on aligned conductive nanofibrous meshes for their synchronized beating. Biomaterials *34*, 1063–1072.

Huebsch, N., Loskill, P., Deveshwar, N., Spencer, C.I., Judge, L.M., Mandegar, M.A., Fox, B.C., Mohamed, T.M.A., Ma, Z., Mathur, A., et al. (2016). Miniaturized iPS-cell-derived cardiac muscles for physiologically relevant drug response analyses. Sci. Rep. *6*, 24726.

Isomura, A., Hörning, M., Agladze, K., and Yoshikawa, K. (2008). Eliminating spiral waves pinned to an anatomical obstacle in cardiac myocytes by high-frequency stimuli. Phys. Rev. E Stat. Nonlin. Soft Matter Phys. *78*, 0662161–0662166.

Jackman, C.P., Carlson, A.L., and Bursac, N. (2016). Dynamic culture yields engineered myocardium with near-adult functional output. Biomaterials *111*, 66–79.

Joanne, P., Kitsara, M., Boitard, S.-E., Naemetalla, H., Vanneaux, V., Pernot, M., Larghero, J., Forest, P., Chen, Y., Menasché, P., et al. (2016). Nanofibrous clinical-grade collagen scaffolds seeded with human cardiomyocytes induces cardiac remodeling in dilated cardiomyopathy. Biomaterials *80*, 157–168.

Kadota, S., Minami, I., Morone, N., Heuser, J.E., Agladze, K., and Nakatsuji, N. (2013). Development of a reentrant arrhythmia model in human pluripotent stem cell-derived cardiac cell sheets. Eur. Heart J. *34*, 1147–1156.

Kamakura, T., Makiyama, T., Sasaki, K., Yoshida, Y., Wuriyanghai, Y., Chen, J., Hattori, T., Ohno, S., Kita, T., Horie, M., et al. (2012). Ultrastructural maturation of human-induced pluripotent stem cell-derived cardiomyocytes in a long-term culture. Circ. J. *77*, 1307–1314.

Karakikes, I., Ameen, M., Termglinchan, V., and Wu, J.C. (2015). Human induced pluripotent stem cell–derived cardiomyocytes: insights into molecular, cellular, and functional phenotypes. Circ. Res. *117*, 80–88.

Kattman, S.J., Witty, A.D., Gagliardi, M., Dubois, N.C., Niapour, M., Hotta, A., Ellis, J., and Keller, G. (2011). Stage-specific optimization of activin/nodal and BMP signaling promotes cardiac differentiation of mouse and human pluripotent stem cell lines. Cell Stem Cell *8*, 228–240.

Kawamura, M., Miyagawa, S., Fukushima, S., Saito, A., Miki, K., Ito, E., Sougawa, N., Kawamura, T., Daimon, T., Shimizu, T., et al. (2013). Enhanced survival of transplanted human induced pluripotent stem cell–derived cardiomyocytes by the combination of cell sheets with the pedicled omental flap technique in a porcine heart. Circulation *128*, S87–S94.

Kharaziha, M., Shin, S.R., Nikkhah, M., Topkaya, S.N., Masoumi, N., Annabi, N., Dokmeci, M.R., and Khademhosseini, A. (2014). Tough and flexible CNT–polymeric hybrid scaffolds for engineering cardiac constructs. Biomaterials *35*, 7346–7354.

Kim, D.-H., Lipke, E.A., Kim, P., Cheong, R., Thompson, S., Delannoy, M., Suh, K.-Y., Tung, L., and Levchenko, A. (2010). Nanoscale cues regulate the structure and function of macroscopic cardiac tissue constructs. Proc. Natl. Acad. Sci. USA *107*, 565–570.

Kimbrel, E.A., and Lanza, R. (2015). Current status of pluripotent stem cells: moving the first therapies to the clinic. Nat. Rev. Drug Discov. *14*, 681–692.

Li, J., Minami, I., Yu, L., Tsuji, K., Nakajima, M., Qiao, J., Suzuki, M., Shimono, K., Nakatsuji, N., and Kotera, H. (2016). Extracellular recordings of patterned human pluripotent stem cell-derived cardiomyocytes on aligned fibers. Stem Cells Int. *2016*, 26340131–26340139.

Lian, X., Zhang, J., Azarin, S.M., Zhu, K., Hazeltine, L.B., Bao, X., Hsiao, C., Kamp, T.J., and Palecek, S.P. (2013). Directed cardiomyocyte differentiation from human pluripotent stem cells by modulating Wnt/β-catenin signaling under fully defined conditions. Nat. Protoc. *8*, 162–175.

Liang, P., Lan, F., Lee, A.S., Gong, T., Sanchez-Freire, V., Wang, Y., Diecke, S., Sallam, K., Knowles, J.W., and Nguyen, P.K. (2013). Drug screening using a library of human induced pluripotent stem cell-derived cardiomyocytes reveals disease specific patterns of cardiotoxicity. Circulation *127*, 1677–1691.

Lin, Y.D., Ko, M.C., Wu, S.T., Li, S.F., Hu, J.F., Lai, Y.J., Harn, H.I.C., Laio, I.C., Yeh, M.L., Yeh, H.I., et al. (2014). A nanopatterned cell-seeded cardiac patch prevents electro-uncoupling and improves the therapeutic efficacy of cardiac repair. Biomater. Sci. *2*, 567–580.

Ma, J., Guo, L., Fiene, S.J., Anson, B.D., Thomson, J.A., Kamp, T.J., Kolaja, K.L., Swanson, B.J., and January, C.T. (2011). High purity human-induced pluripotent stem cell-derived cardiomyocytes: electrophysiological properties of action potentials and ionic currents. Am. J. Physiol. Heart Circ. Physiol. *301*, H2006–H2017.

Mannhardt, I., Breckwoldt, K., Letuffe-Brenière, D., Schaaf, S., Schulz, H., Neuber, C., Benzin, A., Werner, T., Eder, A., Schulze, T., et al. (2016). Human engineered heart tissue: analysis of contractile force. Stem Cell Reports *7*, 29–42.

Masoumi, N., Larson, B.L., Annabi, N., Kharaziha, M., Zamanian, B., Shapero, K.S., Cubberley, A.T., Camci Unal, G., Manning, K., Mayer, J.E., Jr., et al. (2014). Electrospun PGS: PCL microfibers align human valvular interstitial cells and provide tunable scaffold anisotropy. Adv. Healthc. Mater. *3*, 929–939.

Masumoto, H., Matsuo, T., Yamamizu, K., Uosaki, H., Narazaki, G., Katayama, S., Marui, A., Shimizu, T., Ikeda, T., Okano, T., et al. (2012). Pluripotent stem cell-engineered cell sheets reassembled with defined cardiovascular populations ameliorate reduction in infarct heart function through cardiomyocyte-mediated neovascularization. Stem Cells *30*, 1196–1205.

Mathur, A., Ma, Z., Loskill, P., Jeeawoody, S., and Healy, K.E. (2016). In vitro cardiac tissue models: current status and future prospects. Adv. Drug Del. Rev. *96*, 203–213.

Matsa, E., Burridge, P.W., and Wu, J.C. (2014). Human stem cells for modeling heart disease and for drug discovery. Sci. Transl. Med. *6*, 239ps6.

Matsa, E., and Denning, C. (2012). In vitro uses of human pluripotent stem cell-derived cardiomyocytes. J. Cardiovasc. Transl. Res. *5*, 581–592.

Matsa, E., Rajamohan, D., Dick, E., Young, L., Mellor, I., Staniforth, A., and Denning, C. (2011). Drug evaluation in cardiomyocytes derived from human induced pluripotent stem cells carrying a long QT syndrome type 2 mutation. Eur. Heart J. *32*, 952–962.

Memon, I.A., Sawa, Y., Fukushima, N., Matsumiya, G., Miyagawa, S., Taketani, S., Sakakida, S.K., Kondoh, H., Aleshin, A.N., Shimizu, T., et al. (2005). Repair of impaired myocardium by means of implantation of engineered autologous myoblast sheets. J. Thorac. Cardiovasc. Surg. *130*, 1333–1341.

Menasché, P., Vanneaux, V., Fabreguettes, J.-R., Bel, A., Tosca, L., Garcia, S., Bellamy, V., Farouz, Y., Pouly, J., Damour, O., et al. (2015). Towards a clinical use of human embryonic stem cell-derived cardiac progenitors: a translational experience. Eur. Heart J. *36*, 743–750.

Minami, I., Yamada, K., Otsuji, T.G., Yamamoto, T., Shen, Y., Otsuka, S., Kadota, S., Morone, N., Barve, M., Asai, Y., et al. (2012). A small molecule that promotes cardiac differentiation of human pluripotent stem cells under defined, cytokine-and xeno-free conditions. Cell Rep. *2*, 1448–1460.

Nakao, K., Minobe, W., Roden, R., Bristow, M.R., and Leinwand, L.A. (1997). Myosin heavy chain gene expression in human heart failure. J. Clin. Invest. *100*, 2362.

Navarrete, E.G., Liang, P., Lan, F., Sanchez-Freire, V., Simmons, C., Gong, T., Sharma, A., Burridge, P.W., Patlolla, B., Lee, A.S., et al. (2013). Screening drug-induced arrhythmia using human induced pluripotent stem cell–derived cardiomyocytes and low-impedance microelectrode arrays. Circulation *128*, S3–S13.

Nunes, S.S., Miklas, J.W., Liu, J., Aschar-Sobbi, R., Xiao, Y., Zhang, B., Jiang, J., Massé, S., Gagliardi, M., Hsieh, A., et al. (2013). Biowire: a platform for maturation of human pluripotent stem cell-derived cardiomyocytes. Nat. Methods *10*, 781–787.

Orlova, Y., Magome, N., Liu, L., Chen, Y., and Agladze, K. (2011). Electrospun nanofibers as a tool for architecture control in engineered cardiac tissue. Biomaterials *32*, 5615–5624.

Pioner, J.M., Racca, A.W., Klaiman, J.M., Yang, K.-C., Guan, X., Pabon, L., Muskheli, V., Zaunbrecher, R., Macadangdang, J., Jeong, M.Y., et al. (2016). Isolation and mechanical measurements of myofibrils from human induced pluripotent stem cell-derived cardiomyocytes. Stem Cell Reports *6*, 885–896.

Riegler, J., Tiburcy, M., Ebert, A., Tzatzalos, E., Raaz, U., Abilez, O.J., Shen, Q., Kooreman, N.G., Neofytou, E., Chen, V.C., et al. (2015). Human engineered heart muscles engraft and survive long term in a rodent myocardial infarction model. Circ. Res. *117*, 720–730.

Robertson, C., Tran, D.D., and George, S.C. (2013). Concise review: maturation phases of human pluripotent stem cell-derived cardiomyocytes. Stem Cells *31*, 829–837.

Schwan, J., Kwaczala, A.T., Ryan, T.J., Bartulos, O., Ren, Y., Sewanan, L.R., Morris, A.H., Jacoby, D.L., Qyang, Y., Campbell, S.G., et al. (2016). Anisotropic engineered heart tissue made from laser-cut decellularized myocardium. Sci. Rep. *6*, 32068.

Shao, Y., Sang, J., and Fu, J. (2015). On human pluripotent stem cell control: the rise of 3D bioengineering and mechanobiology. Biomaterials *52*, 26–43.

Shiba, Y., Fernandes, S., Zhu, W.-Z., Filice, D., Muskheli, V., Kim, J., Palpant, N.J., Gantz, J., Moyes, K.W., Reinecke, H., et al. (2012). Human ES-cell-derived cardiomyocytes electrically couple and suppress arrhythmias in injured hearts. Nature *489*, 322–325.

Shiba, Y., Gomibuchi, T., Seto, T., Wada, Y., Ichimura, H., Tanaka, Y., Ogasawara, T., Okada, K., Shiba, N., Sakamoto, K., et al. (2016). Allogeneic transplantation of iPS cell-derived cardiomyocytes regenerates primate hearts. Nature *538*, 388–391.

Shinozawa, T., Nakamura, K., Shoji, M., Morita, M., Kimura, M., Furukawa, H., Ueda, H., Shiramoto, M., Matsuguma, K., Kaji, Y., et al. (2017). Recapitulation of clinical individual susceptibility to drug-induced QT prolongation in healthy subjects using iPSC-derived cardiomyocytes. Stem Cell Reports *8*, 226–234.

Snir, M., Kehat, I., Gepstein, A., Coleman, R., Itskovitz-Eldor, J., Livne, E., and Gepstein, L. (2003). Assessment of the ultrastructural and proliferative properties of human embryonic stem cell-derived cardiomyocytes. Am. J. Physiol. Heart Circ. Physiol. *285*, H2355–H2363.

Tanaka, M., Isomura, A., Hörning, M., Kitahata, H., Agladze, K., and Yoshikawa, K. (2009). Unpinning of a spiral wave anchored around a circular obstacle by an external wave train: common aspects of a chemical reaction and cardiomyocyte tissue. Chaos *19*, 043114.

Van Kooten, T.G., Whitesides, J.F., and Von Recum, A.F. (1998). Influence of silicone (PDMS) surface texture on human skin fibroblast proliferation as determined by cell cycle analysis. J. Biomed. Mater. Res. *43*, 1–14.

Weinberger, F., Breckwoldt, K., Pecha, S., Kelly, A., Geertz, B., Starbatty, J., Yorgan, T., Cheng, K.-H., Lessmann, K., Stolen, T., et al. (2016). Cardiac repair in Guinea pigs with human engineered heart tissue from induced pluripotent stem cells. Sci. Transl. Med. *8*, 363ra148.

Xu, C., Wang, L., Yu, Y., Yin, F., Zhang, X., Jiang, L., and Qin, J. (2017). Bioinspired onion epithelium-like structure promotes the maturation of cardiomyocytes derived from human pluripotent stem cells. Biomater. Sci. *5*, 1810–1819.

Yang, X., Pabon, L., and Murry, C.E. (2014). Engineering adolescence maturation of human pluripotent stem cell–derived cardiomyocytes. Circ. Res. *114*, 511–523.

Yu, J., Lee, A.R., Lin, W.H., Lin, C.W., Wu, Y.K., and Tsai, W.B. (2014). Electrospun PLGA fibers incorporated with functionalized biomolecules for cardiac tissue engineering. Tissue Eng. Part A. *20*, 1896–1907.

Zong, X., Bien, H., Chung, C.-Y., Yin, L., Fang, D., Hsiao, B.S., Chu, B., and Entcheva, E. (2005). Electrospun fine-textured scaffolds for heart tissue constructs. Biomaterials *26*, 5330–5338.

Zwi, L., Caspi, O., Arbel, G., Huber, I., Gepstein, A., Park, I.-H., and Gepstein, L. (2009). Cardiomyocyte differentiation of human induced pluripotent stem cells. Circulation *120*, 1513–1523.

Stem Cell Reports, Volume *9*

Supplemental Information

Human Pluripotent Stem Cell-Derived Cardiac Tissue-like Constructs for Repairing the Infarcted Myocardium

Junjun Li, Itsunari Minami, Motoko Shiozaki, Leqian Yu, Shin Yajima, Shigeru Miyagawa, Yuji Shiba, Nobuhiro Morone, Satsuki Fukushima, Momoko Yoshioka, Sisi Li, Jing Qiao, Xin Li, Lin Wang, Hidetoshi Kotera, Norio Nakatsuji, Yoshiki Sawa, Yong Chen, and Li Liu

Supplementary Materials for

Human Pluripotent Stem Cell-Derived Cardiac Tissue-Like Constructs for Repairing of the Infarcted Myocardium

Junjun Li†[a, b], Itsunari Minami†[a, c], Motoko Shiozaki[c], Leqian Yu[a, b], Shin Yajima[c], Shigeru Miyagawa[c], Yuji Shiba[d], Nobuhiro Morone[a, §], Satsuki Fukushima[c], Momoko Yoshioka[a], Sisi Li[a, e], Jing Qiao[a,b], Xin Li[a], Lin Wang[a], Hidetoshi Kotera[b], Norio Nakatsuji[a], Yoshiki Sawa[c]*, Yong Chen[a, e]*, Li Liu[a, b]*

Supplemental experimental procedures

Nanofiber Fabrication

Poly(D,L-lactic-co-glycolic acid) (PLGA, 75/25, Sigma, USA) was mixed with tetrahydrofuran (THF, Wako, Japan) at different concentrations: 20%, 23%, and 25% (w/v); then, ionic surfactant sodium dodecyl sulphate (SDS, Wako, Japan) dissolved in de-ionized water was added to a final concentration of 0.92 g L^{-1}. For fluorescent labeling, PLGA solution was loaded with fluorescein isothiocyanate (FITC) or Alexa Fluor® 594 (Life Technologies, USA). PLGA nanofibers were fabricated by electrospinning at the voltage of 10 kV provided by a DC high-voltage generator (Tech Dempaz, Japan). The solution was loaded into a 1-mL syringe to which a needle with a 0.6-mm inner diameter was attached; the positive electrode of the high-voltage power supply was connected to the needle. A grounded rotating drum was used at the speed of 11.4 m s^{-1} to generate aligned nanofibers (ANFs); random nanofibers (RNFs) were generated without rotation. The thickness of nanofibers was controlled by varying the spin time: 10 min for high-density ANFs (H-ANFs, 11.3 ± 1.2 μm), 40 s for low-density ANFs (L-ANFs, 1.5 ± 0.1 μm) and 20 s for RNFs (1.5 ± 0.1 μm). The distance between the tip and collector was maintained at 8 cm. Before spinning, a layer of aluminium foil was attached to the drum for the fiber transfer procedure. Nanofibers were collected in the aluminium foil which was then peeled off and pressed onto the substrate by a thermal press machine (AS ONE, Japan) or transferred to a poly-dimethylsiloxane (PDMS) frame (1 × 1 cm^2); then, the foil was removed and nanofibers remained on the substrate or PDMS frame.

Electrophysiological Characterization

Extracellular recording of field potentials (FPs) was performed using the multielectrode array (MEA) data acquisition system (USB-ME64-System, Multi Channel Systems, Germany).

Signals were recorded from day 2 after CM seeding. The data were collected and processed using MC_Rack (Multi Channel Systems) or LabChart (ADInstruments, New Zealand).

Electrical activation was started by applying bipolar stimuli (±1500 mV, 40 μs) in the electrodes at the MEA centre. The local activation time (LAT) for a single electrode was determined by calculating the minimum of the first derivative plot of the original data. The isochronal map was constructed based on linear interpolation between the electrodes (Meiry et al., 2001), calculated using the Matlab function (Matlab, MathWorks, America). The amplitude, QT interval, and beating rate were determined by analyzing the wave form, and the corrected cQT interval was calculated by normalization to the CM beating rate using the Fridericia correction formula: cQT interval = QT interval/$\sqrt[3]{\text{RR interval}}$. To assess the effects of different drugs, E-4031, isoproterenol, propranolol, Verapamil and Quinidine were added to 1 mL of medium respectively between 6-14 day after cell seeding.

Electron Microscopy

Top view high-resolution images were obtained using a scanning electron microscope (SEM JCM-5000; JEOL Ltd., Japan) operating at 10 kV. CM samples were fixed with 4% paraformaldehyde (PFA; Wako) for 2 min at room temperature, washed twice with PBS, immersed in 30% ethanol for 30 min, and dehydrated in a series of ethanol concentrations (50%, 70%, 80%, 90%, and 100%) for 10 min per each step, followed by nitrogen drying. A 5-nm-thick platinum layer was deposited on the samples by sputtering (MSP 30T; Shinku Device, Japan).

For transmission electron microscopy (TEM), the samples were fixed with 2% glutaraldehyde (Distilled EM Grade, Electron Microscopy Sciences, USA) in NaHCa buffer (100 mM NaCl, 30 mM HEPES, 2 mM $CaCl_2$, adjusted to pH 7.4 with NaOH) and successively post-fixed

with 0.25% OsO4/0.25% $K_4Fe(CN)_6$, then with 1% tannic acid, and finally with 50 mM uranyl acetate. The samples were washed, dehydrated in a series of ethanol, and embedded in TABA EPON 812 resin (TAAB Laboratories Equipment Ltd, UK). After polymerization at 65°C, ultrathin sections (60–100 nm) were cut perpendicular to PLGA fibers using an ultramicrotome (Leica FC6, Austria), mounted on EM grids, stained with lead citrate, and analyzed by TEM (JEOL JEM1400, Japan).

Histology

Tissues were washed three times with PBS, fixed in 4% PFA in PBS, and embedded in paraffin. Thin sections were cut, stained with hematoxylin and eosin (Muto chemical corporation, Japan). Capillary density and inflammatory reactions were assessed by immunohistolabeling for CD31 (mouse monoclonal IgG, 1:50; Dako: M0823) or CD68 (mouse monoclonal IgG, 1:100; Abcam: 955) respectively. The sections were observed under a CKX41 microscope (Olympus) or a BIOREVO fluorescence microscope (KEYENCE Corporation).

Immunostaining and Imaging

CMs were fixed in 4% PFA at room temperature for 30 min, permeabilized with 0.5% v/v Triton X-100 in Dulbecco's (D)-PBS at room temperature for 1 h, and incubated in blocking solution (5% v/v normal goat serum, 5% v/v normal donkey serum, 3% v/v bovine serum albumin, and 0.1% v/v Tween 20 in D-PBS) at 4°C for 16 h. CMs were then incubated with primary antibodies: anti-β-MHC (mouse monoclonal IgM, 1:100; Santa Cruz Biotechnology: SC-53089), anti-α-actinin (mouse monoclonal IgG, 1:1000; Sigma: A7811), and anti-cTnT (mouse monoclonal IgG, 1:200; Santa Cruz Biotechnology: SC-20025) at 4°C for 16 h. Cells were washed and incubated with appropriate secondary antibodies diluted 1:300 in blocking

buffer: DyLight-594 anti-mouse IgM (Jackson ImmnoResearch: 715-516-020), Alexa Fluor 594 anti-rabbit IgG (Jackson ImmnoResearch: 711-586-152), Alexa Fluor 594 anti-mouse IgG (Jackson ImmnoResearch: 715-586-150), and Alexa Fluor 488 anti-rabbit IgG (Jackson ImmnoResearch: 711-546-152) at room temperature for 1 h. Cell were counterstained with 300 nM 4'-6-diamidino-2-phenylindole (DAPI, Wako) at room temperature for 30 min to visualize the nuclei. Images were captured using a fluorescent or confocal microscopes (Olympus), and the orientation of CMs and nanofibers was evaluated by the Fourier component analysis using the ImageJ Directionality plugin (Woolley et al., 2011) which assessed the orientation distribution for each color channel. Tomography images were acquired and combined to form 3D images using the Optical Coherence Microscopy system and the white-light Linnik interferometer (OCM system, Panasonic).

For immunostaining after transplantation, tissues were rinsed with PBS, cut, immersed in 30% sucrose in PBS, and embedded in O.C.T. compound (Sakura Finetek USA, Inc.). Frozen sections were cut into 7-μm-thick slices using a cryostat (Leica CM 1950) and mounted on MAS-coated glass slides (Matsunami Glass Ind. Ltd.). After treatment with PBS or Tris-buffered saline (TBS) containing 1% bovine serum albumin (BSA) and 0.05% Tween 20, the sections were incubated with a mouse anti-cardiac troponin T antibody (2–10 μg/mL; Abcam Plc: ab8295), a rabbit anti-cardiac troponin I (rabbit monoclonal IgG, 1:100; Abcam Plc: ab52862) or a mouse anti-human nuclear antibody (HNA) (mouse monoclonal IgG, 1:200; MED Millipore: MAB1281) for 16 h at 4°C, followed by incubation with secondary anti-mouse Alexa 555-conjugated IgG (1:200; Life Technologies: A21422), anti-rabbit Alexa 555-conjugated IgG (1:200; Life Technologies: A21428), anti-mouse Alexa 488-conjugated IgG (1:200; Life Technologies: A11001) and anti-rabbit Alexa 488-conjugated IgG (1:200; Life Technologies: A11008). F-actin was stained using Alexa Fluor 647-labelled phalloidin (1:100; Life Technologies: A22287). The sections were mounted with the

ProLong Gold antifade reagent with DAPI (Life Technologies) and examined under a confocal laser scanning microscope (FV1200; Olympus Co.) at the excitation wavelengths of 405, 488, 543, and 635 nm.

Flow Cytometry

HiPSCs-CMs cultured on different substrates were harvested using TrypLE Express solution (Life Technologies), fixed in 4% PFA at room temperature for 30 min, permeabilized with 0.5% v/v Triton X-100 in Dulbecco′s (D)-PBS at room temperature for 30 min, incubated with anti-cTnT antibodies (mouse monoclonal IgG, 1:200; Santa Cruz Biotechnology: SC-20025) or isotype-matched antibodies (BD Phosphoflow: 557782) at 37 ◦C for 30 min, washed with D-PBS, and incubated with Alexa Fluor 488 anti-mouse IgG (1:500; Jackson ImmnoResearch: 715-546-150). Cells were then washed twice with D-PBS and analyzed using a FACS Canto II flow cytometer (BD Biosciences, USA) and the FlowJo software (Treestar Inc., USA). Data shown are representative of at least three independent experiments.

qPCR

Total RNA was harvested using Trizol (Life Technologies), and RNA concentration was measured using a NanoDrop1000 spectrophotometer (Thermo Fisher Scientific, USA). cDNA was synthesized and analyzed by qPCR using the SYBR Green PCR MasterMix (Life Technologies) and the qBiomarker Validation PCR Array (IPHS-102A; Qiagen, USA) in a 96-well format following the manufacturer's instructions. The cycling conditions were as follows: initial denaturation at 95°C for 10 min, followed by 40 cycles at 95°C for 15 s and 60°C for 1 min; the reactions were performed in a StepOnePlus Real-Time PCR system (Life Technologies). The gene expressions were measured by ddCt method relative to house keep

gene (GAPDH). Heatmaps were generated by the R package open-source software for bioinformatics. The clustering order was produced with Ward.D clustering algorithm.

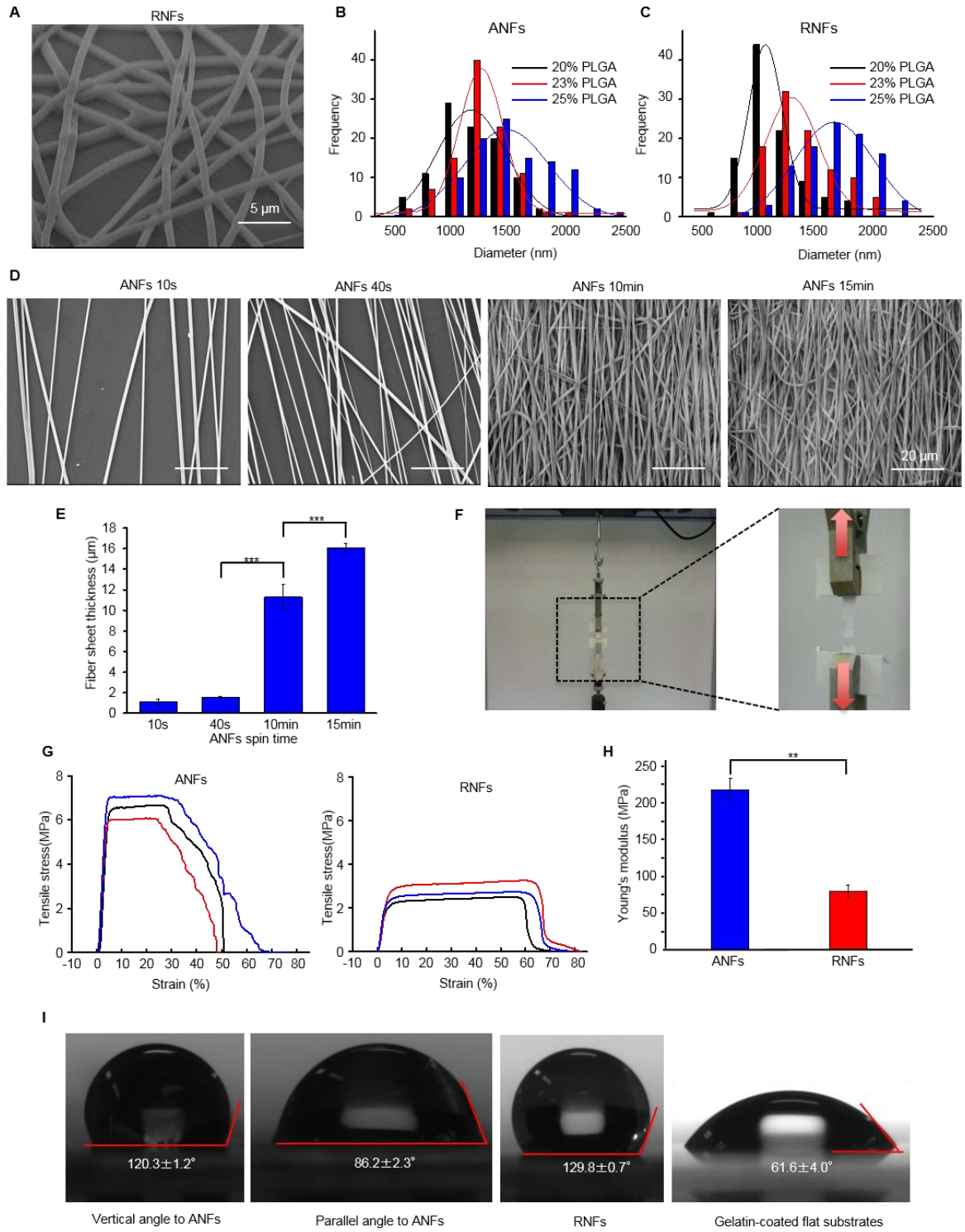

Figure S1. Characteristics of nanofibers. Related to Figure 1. (A) A representative electron microscopy image of randomly arranged nanofibers (RNFs). **(B, C)** Diameter distribution of aligned nanofibers (ANFs, **B**) and RNFs **(C)** fabricated with different concentrations of poly(D,L-lactic-co-glycolic acid) (PLGA). **(D)** Electron microscopy images

of ANFs manufactured using different spin times (10 s, 40 s, 10 min, and 15 min). **(E)** ANFs thickness depending on the spin time. Data are represented as means ± SD, n = 4 independent experiments. ***p < 0.001 by One-way ANOVA followed by Tukey's post hoc test. **(F)** Photographs of the experimental setup. Specimen gauge length and width were determined using a Shimadzu Autograph AGS-X micro-tensile tester (Shimadzu Corp.) with a 1N load cell and digital video extensometer, setting the cross-head speed at 10 mm min^{-1}. The rigidity was calculated using Trapezium X with an initial linear region of the stress-strain curve. **(G)** Stress-strain curves of aligned nanofibers (ANFs) and random nanofibers (RNFs). **(H)** Young's modulus of ANFs and RNFs. Data are represented as means ± SD, n = 3 independent experiments. **p < 0.01 by Student's t test. **(I)** Contact angle measurement of ANF/RNF and gelatin-coated flat substrates. The sessile drop method was used to measure the contact angle of a water droplet on the substrate using a microscope with a CCD camera. A 2-μL water droplet was deposited onto the substrate and the water/substrate interface was photographed. The edge of the droplet was then analyzed using a sessile drop-fitting model. Data are represented as means ± SD, n = 3 independent experiments.

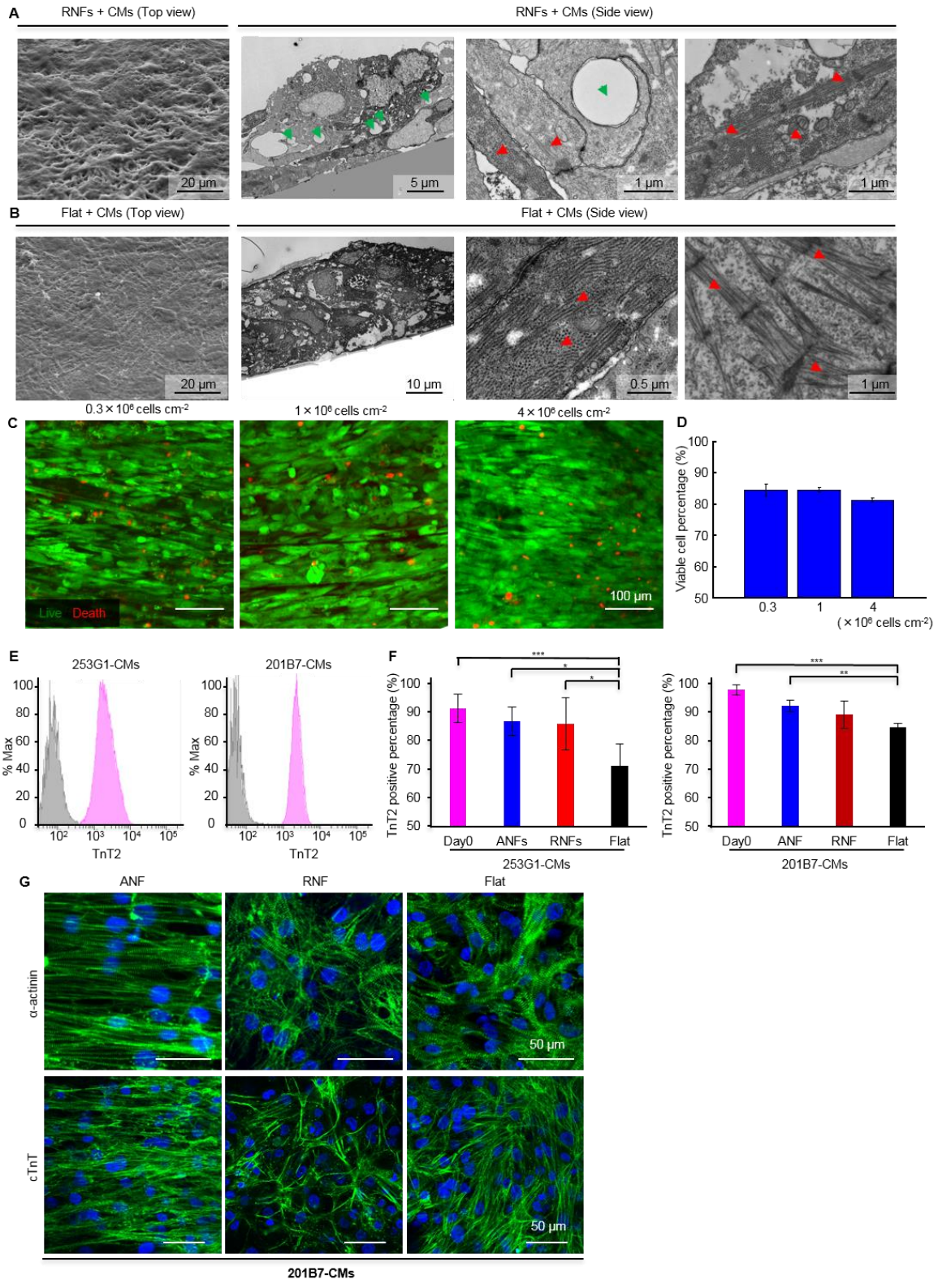

Figure S2. Tissue formed on different substrates. Related to Figure 1 and Figure 2. (A) Scanning electron microscopy **(**SEM, top view) and transmission electron microscopy (TEM, side view) images of cardiomyocytes (CMs) cultured on random nanofibers (RNFs) for 14 days. **(B)** SEM (top view) and TEM (side view) images of CMs cultured on Flat for 14 days. The green and red arrows indicate nanofibers and sarcomeric bundles in the actin-myosin system, respectively. **(C, D)** Viability of CTLCs with different cell densities on day 6. Data

are represented as means ± SD, n = 3 independent experiments. **(E)** Flow cytometry data of cTnT positive cell (hiPS cell line: 253G1; 201B7) on day 0. **(F)** Flow cytometry analysis of CMs on different substrates: aligned nanofibers (ANFs), random nanofibers (RNFs), and gelatin-coated flat substrate (Flat) for 14 days. Data are represented as means ± SD. For 253G1**,** Day 0: n = 32; ANFs: n = 3; RNFs: n = 3; Flat: n = 3; For 201B7, n = 3 (n represents independent experiments for all the groups). *$p<0.05$, **$p<0.01$ and ***$p < 0.001$ by One-way ANOVA followed by Tukey's post hoc test. **(G)** Immunostaining images of α-actinin and cTnT (green). Cardiomyocytes (CMs, 201B7) were cultured on different substrates for 14 days.

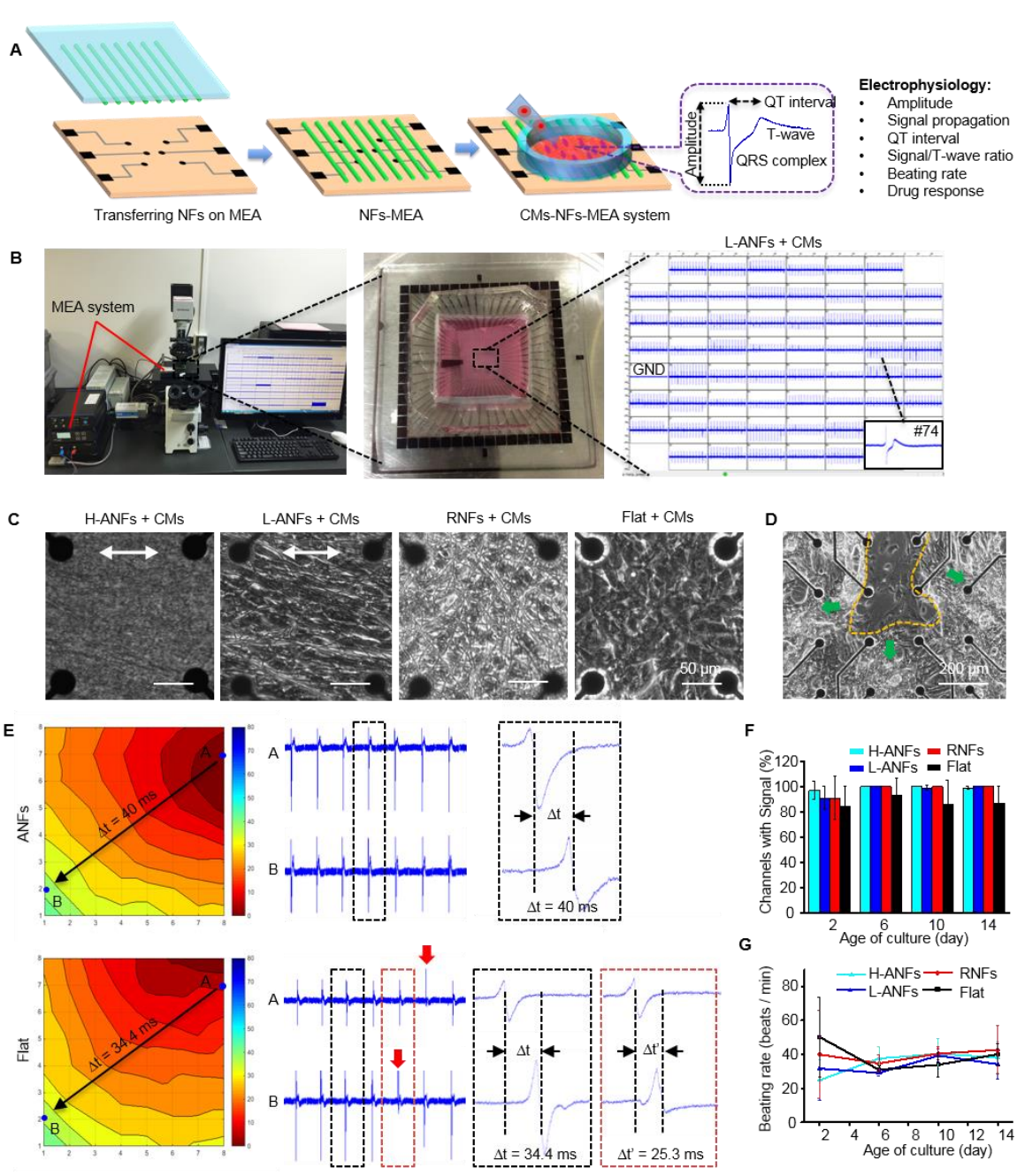

Figure S3. Extracellular recording of cardiomyocytes (CMs) using the microelectrode array (MEA). Related to Figure 3. (A) Schematic representation of cardiac tissue-like construct (CTLC) integration into the MEA system. The encircled image is a representative electrogram of the field potential (FP) recorded from CMs, illustrating the parameters to be analyzed. **(B)** Images of the MEA system and MEA chip with CTLC. The enlarged images indicate the homogeneous electrical signals recorded by electrodes. **(C)** Phase contrast images of CMs on different substrates: high-density and low-density aligned nanofibers (H-ANFs and L-ANFs, respectively), random nanofibers (RNFs), and gelatin-coated flat substrates (Flat). The white arrows mark ANFs orientation. **(D)** Images of the Flat sample on day 6 with CMs clusters marked by green arrows. The dashed line marks the area with few remaining CMs. **(E)** Homogeneity and regularity of CM beating on ANFs and Flat. Activation maps (left) illustrate homogeneous propagation of spontaneous contractions; contraction regularity is shown by a series of beatings (right) recorded from point A to B, with a delay of Δt. The red arrows mark irregular beating which resulted in different Δt = 25.3

ms. **(F)** Channels recording field potential (n = 6–8 independent biological replicates). **(G)** CM beating rate at different culture times (n = 3–5 independent biological replicates). Data are represented as means ± SD.

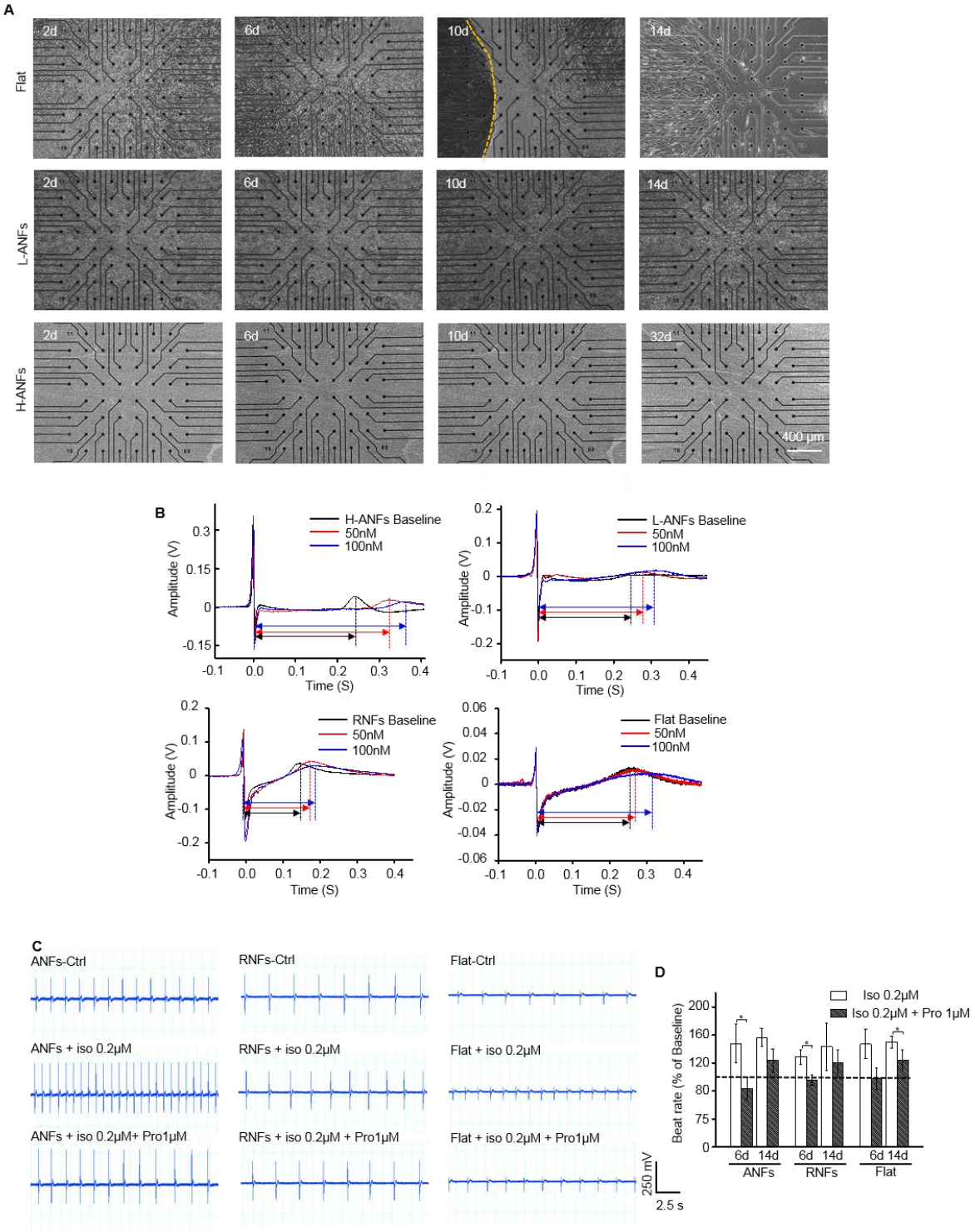

Figure S4. Long term culture and drug effects on cardiomyocytes (CMs). Related to Figure 3. (A) Long-term culture of cardiomyocytes (CMs) on gelatin-coated flat substrates (Flat) and low-density and high-density aligned nanofibers (L-ANFs and H-ANFs, respectively). The dashed line marks the area where the CM sheet peeled off from the

substrates; the CM sheet totally peeled off from Flat on day 14. Cardiac tissue-like constructs (CTLCs) created on H-ANFs were sustained for over 32 days. **(B)** Prolongation of the repolarization phase after E4031 application. **(C)** Representative beating of CMs treated with isoproterenol (Iso) and propranolol (Pro) and cultured on different substrates. **(D)** Effects of Iso and Pro on CM beating rate. Data are represented as means ± SD, n = 3–4 independent biological replicates. *p < 0.05 by Student's t test.

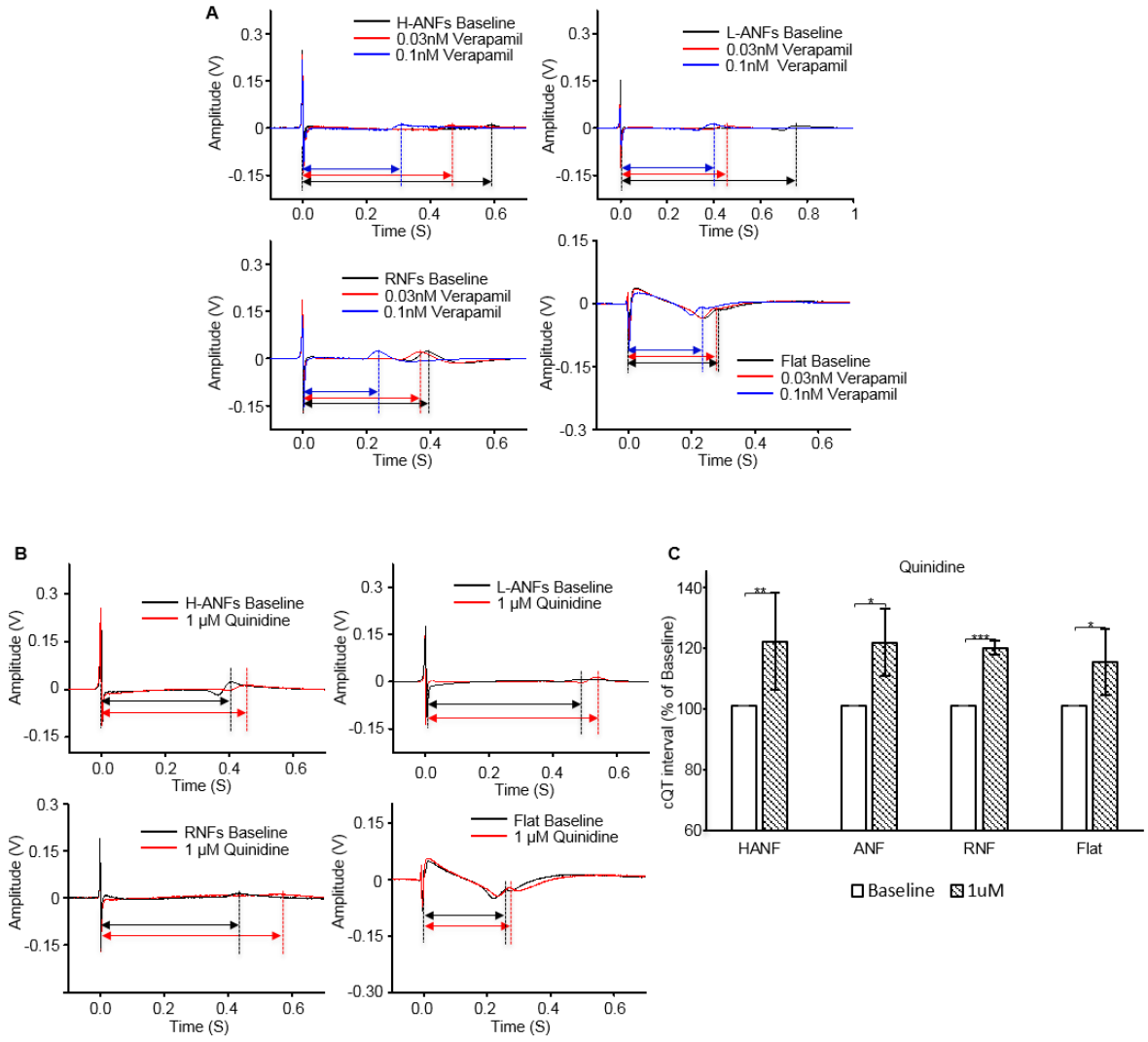

Figure S5. Drug effects on cardiomyocytes (CMs). Related to Figure 3. (A) Shortening of the repolarization phase after verapamil application. **(B)** Prolongation of the repolarization phase after quinidine application. **(C)** Effects of quinidine on corrected QT interval (cQT interval) of CM beating. Data are represented as means ± SD, n = 3–7 independent biological replicates. *p < 0.05, **p < 0.01, and ***p < 0.001 by Student's t test.

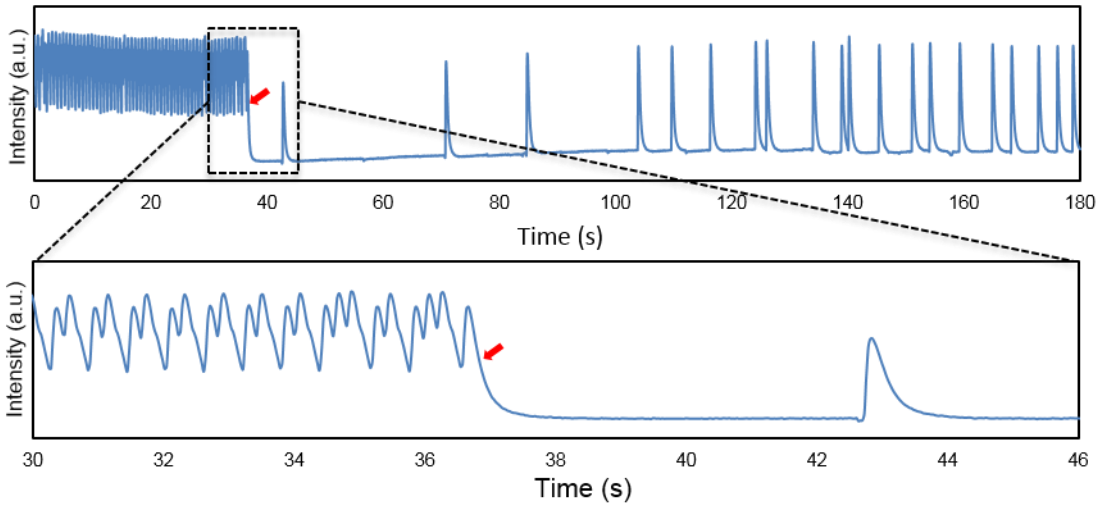

Figure S6 Ca^{2+} transients of the GCaMP3-positive CTLC on a host CM sheet with spiral waves. Related to Figure 4. The recording lasted for 3 min and the red arrow marked the moment when the spiral wave was terminated by the coupling of CTLC with the host CM sheet.

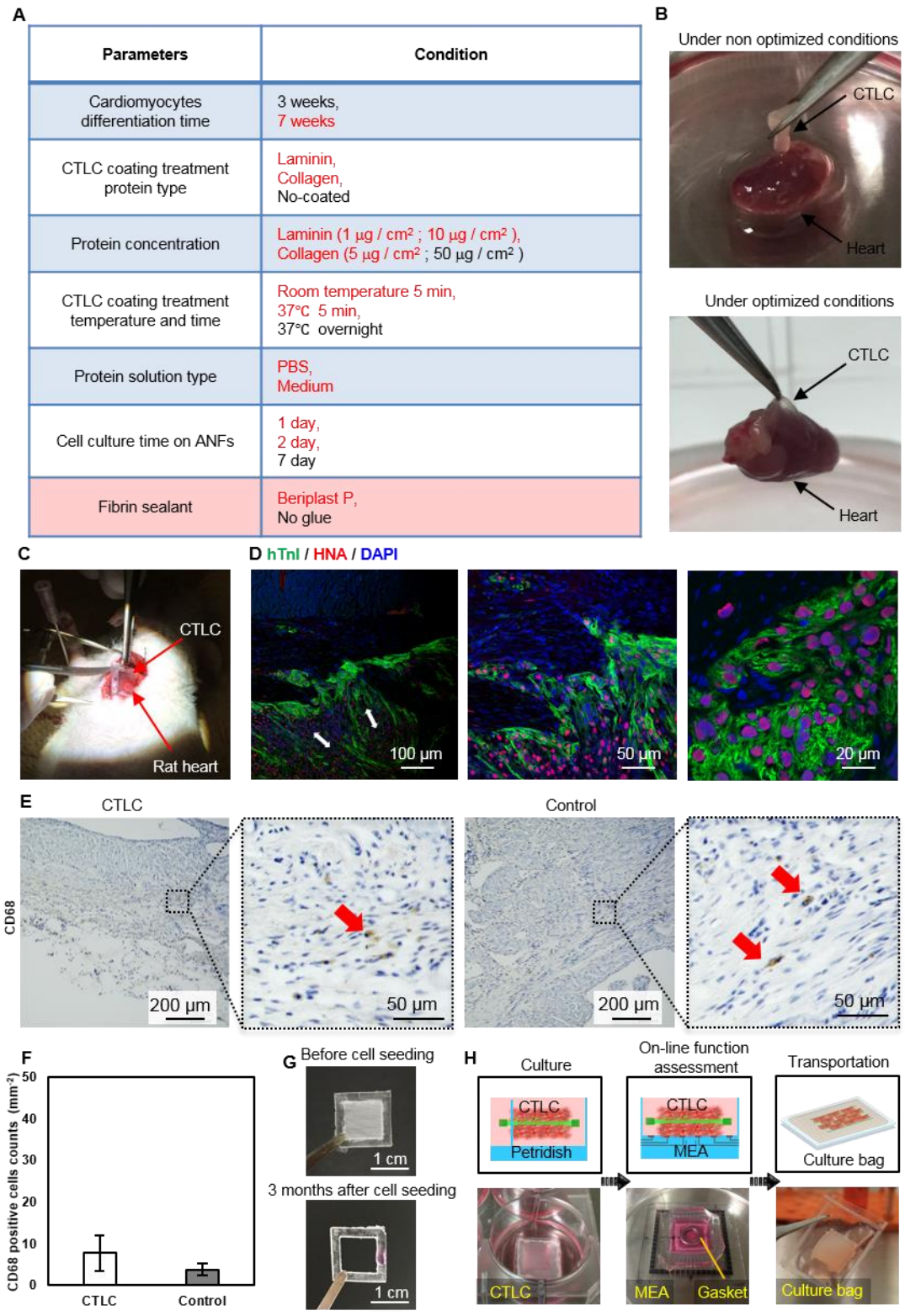

Figure S7. Preparation of a cardiac tissue-like construct (CTLC) for transplantation). Related to Figure 5 and Figure 6. (A) Condition screening by the *in vitro* attachment to mouse hearts. To improve CTLC attachment to the heart, a number of experimental conditions were screened. The conditions marked in red were used for transplantation. **(B)** CTLC attachment was assessed *in vitro* by testing whether the mouse heart-bound CTLC could sustain the weight of the heart. **(C)** Transplantation of CTLC on a rat heart**. (D)** Double immunostaining of consecutive sections from the *in vivo* transplanted CTLC for human

cardiac troponin I (hTnI) and human nuclear antigen (HNA); nuclei were stained with DAPI. The white arrow indicated the alignment of CMs. **(E)** Long-term degradation of nanofibers. Aligned nanofibers (ANFs) were mounted onto a PDMS frame (top) and immersed in medium after seeding of cardiomyocytes (CMs); ANFs would degrade within 3 month (bottom). **(E)** Immunohistochemical analysis on peri-ischemic zone in MI heart 4 week after transplantation of CTLC (left) and acellular control (right). The sections are immunostained with CD68 antibodies. The red arrow marked the CD68-positive cells. **(F)** The CD68 positive cells density in CTLC and control group. Data are represented as means ± SD, n = 3 rats. **(G)** Preparation and transport of the CTLC. After cell seeding, the CTLC can be functionally evaluated before transportation and used for other applications. A gasket is used to fix the CTLC on the MEA for signal recording.

REFERENCES

Meiry, G., Reisner, Y., Feld, Y., Goldberg, S., Rosen, M., Ziv, N., Binah, O. (2001). Evolution of action potential propagation and repolarization in cultured neonatal rat ventricular myocytes. J. Cardiovasc. Electrophysiol. *12*, 1269-1277.

Woolley, A.J., Desai, H.A., Steckbeck, M.A., Patel, N.K., Otto, K.J. (2011). In situ characterization of the brain-microdevice interface using device-capture histology. J. Neurosci. Methods *201*, 67-77.